



Apatite texture and composition in the Tonglushan porphyry-related skarn system, eastern China: Implications for mineral exploration

Fei Zhang^{a,b}, Ben J. Williamson^{a,*}, Sam Broom-Fendley^a

^a Camborne School of Mines, University of Exeter, Penryn, Cornwall TR10 9FE, United Kingdom

^b Zhengzhou Institute of Multipurpose Utilization of Mineral Resources, CAGS, Zhengzhou 450006, China



ARTICLE INFO

Keywords:

Apatite
Cathodoluminescence
Porphyry-skarn deposits
Endoskarn
Exoskarn
Tonglushan

ABSTRACT

The composition of 'indicator' minerals is thought to provide a guide to the potential of magmatic arc systems to form porphyry Cu deposits, but whether this is also the case for endoskarn- and exoskarn-dominated systems remains unclear, despite their importance as a source of Cu, Fe and Au. In a first step to address this, we compare the texture, cathodoluminescence (CL) colour and composition of apatite between relatively fresh quartz monzonodiorite (QMD) and porphyry-type-, endoskarn- and Fe-(Cu)-mineralised exoskarn components of the Tonglushan porphyry-skarn system of the Daye ore district, China. In the relatively fresh QMD, apatite luminesces yellow-green due to elevated Mn contents. However, where affected by potassio-sodic alteration, it shows green-blue CL thought to reflect partial removal of Mn and an associated increase in REE. Apatite in the endoskarn is more pervasively replaced and veined, and shows mid-blue luminescence due to relatively low Mn, Mg and Cl. The exoskarns contain apatite with variable grain shapes and navy blue-violet or bright to dark blue CL colours, caused by low Mn and elevated Ce, and with only small patches of pale yellow-green CL. Apatite is near absent in the limestone wall rocks and xenoliths and, therefore, where present in the exoskarns is interpreted to have precipitated from the same fluids as the Fe-(Cu) mineralization.

Apatite CL colour and chemistry is indicative of the different styles of alteration and mineralisation in the Tonglushan system and provides insights into the composition of skarn-forming fluids. Our results offer a potentially effective method for utilising apatite as a porphyry and skarn deposit indicator mineral in a range of exploration materials including regolith and stream sediments.

1. Introduction

There have been numerous attempts to develop indicator minerals to identify magmatic intrusions capable of hosting porphyry Cu mineralisation. The advantages they offer include ease and low environmental impact of collection and analysis and the possibility to analyse material from plutonic and volcanic rocks, and surficial sediments (if resistant to weathering and erosion) (Cooke et al., 2017; Wilkinson et al., 2017). Examples of investigated minerals in porphyry Cu systems include apatite (e.g., Bouzari et al., 2016; Mao et al., 2016; Zhu et al., 2022), magnetite (e.g., Dupuis and Beaudoin, 2011; Huang et al., 2019; Bédard et al., 2022), zircon (e.g., Lu et al., 2016; Loader et al., 2017; Lee et al., 2021), chlorite (e.g., Wilkinson et al., 2015; Pacey et al., 2020) and plagioclase (Williamson et al., 2016; 2018). Less attention has been given to the development of indicator minerals to discriminate ore systems where endoskarns rather than porphyry-style mineralisation

predominate. Importantly, endoskarns and porphyry Cu deposit are often mutually exclusive, regardless of whether an endoskarn is poorly or heavily mineralised (e.g., Chang et al., 2015; Einaudi and Burt, 1982; Meinert et al., 2005; Zhang et al., 2023).

Apatite has been extensively investigated as an indicator mineral as it is common in volcanic and plutonic rocks hosting porphyry and skarn deposits, as well as their associated hydrothermal systems, and it can accommodate a wide variety of substituting elements (Pan and Fleet, 2002; Piccoli and Candela, 2002; Webster and Piccoli, 2015). Variations in trace element concentrations in apatite have been used to interpret complex magmatic processes (e.g., Boyce and Hervig, 2009; Nathwani et al., 2020), sulphur evolution (e.g., Streck and Dilles, 1998; Economos et al., 2017), and magma oxidation state (Miles et al., 2014; Konecke et al., 2017; Bromiley, 2021).

The composition of primary apatite in hydrothermal systems is influenced by the nature of the fluids, fluid-mineral and

* Corresponding author.

E-mail address: b.j.williamson@exeter.ac.uk (B.J. Williamson).

mineral–mineral element partitioning, and compositional features inherited from the protolith (Belousova et al., 2002; Harlov, 2015; Kusebauch et al., 2015; Andersson et al., 2019; Palma et al., 2019; Zheng et al., 2022), and it is susceptible to modification as a result of interaction with aqueous fluids of varying salinity and proportions of CO₂, HCl, H₂SO₄ and/or F (Harlov et al., 2002, 2005, 2007; Harlov and Forster, 2003). It has therefore been used to assess hydrothermal and mineralising processes in porphyry (Bouzari et al., 2016; Brugge et al., 2017; Cao et al., 2021; Qu et al., 2022), exoskarn (Zhang et al., 2021b; Zhou et al., 2022), iron oxide-copper-gold (IOCG) (Mercer et al., 2020), iron oxide-apatite (IOA) (Harlov et al., 2016), and carbonatite and alkaline rocks with associated REE deposits (Broom-Fendley et al., 2016; Decrée et al., 2020; Lu et al., 2021), and to discriminate different types of ore deposits (Cao et al., 2012; Mao et al., 2016).

Internal apatite textures can be revealed using backscattered electron (BSE) and CL imaging and X-ray element mapping. Textural variations can indicate multiple stages of magmatic and/or hydrothermal processes related to alteration and mineralisation and may provide a vectoring tool in mineral exploration (Bouzari et al., 2016; Chakhmouradian et al., 2017; Baele et al., 2019; Cao et al., 2021). Examples include exploration for REE and phosphate deposits related to alkaline and carbonatite complexes (Campbell and Henderson, 1997; Kempe and

Götze, 2002; Broom-Fendley et al., 2016, 2021; Chakhmouradian et al., 2017; Decrée et al., 2020; Lu et al., 2021). Despite the large number of studies of apatite in the above environments, there have been few on the textural and chemical characteristics of apatite in skarns, with one notable example being the Mactung W exoskarn, Canada (Roy-Garand, 2019).

The aim of our study is to assess whether textural, CL colour and chemical properties of apatite can be used to distinguish endoskarns, exoskarns and porphyry-styles of alteration. To address this question, we focus on the Tonglushan QMD porphyry-related skarn system in the Daye ore district of eastern China. This was ideally suited to the study as it hosts a large Cu-Fe-(Au) exoskarn deposit containing proven reserves of 1.08 Mt Cu (1.78% Cu), 60 Mt Fe (41.1% Fe), 70 t Au and 508 t Ag, and extensive but generally ‘barren’ endoskarns and uneconomic porphyry-style mineralization. In addition, the mineralogy, geochemistry, oxygen isotope and fluid inclusion characteristics of the endo- and exoskarns are already well documented in the literature (Xie et al., 2011; Zhang et al., 2020; Zhao et al., 1990, 2012; Zhou et al., 2022).

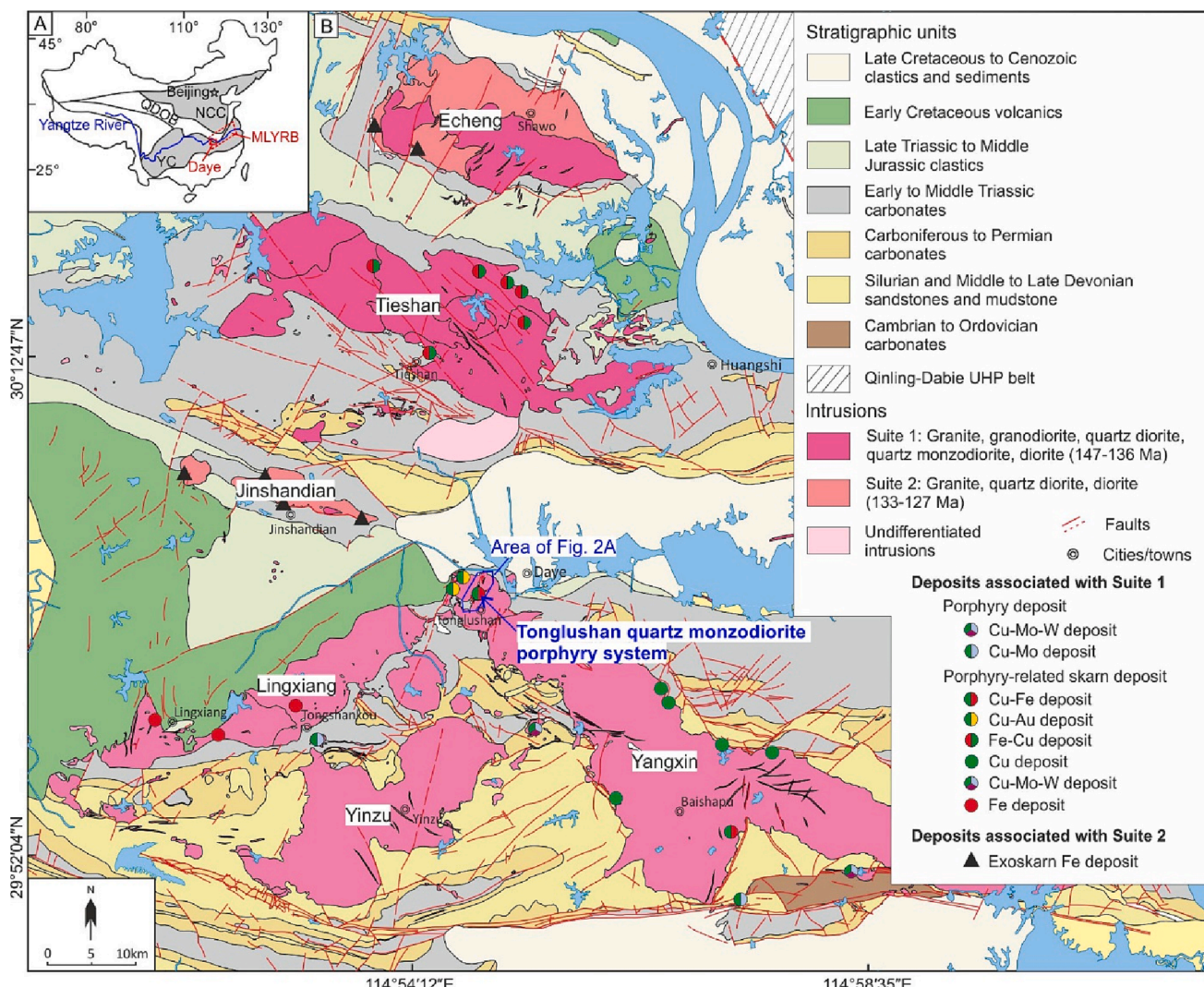


Fig. 1. (A) Map of China showing the location of the Middle-Lower Yangtze River metallogenic belt (MLYRB) and the Daye District (modified after Li et al., 2014). (B) Simplified geological map of the Daye ore district showing the main stratigraphic units, intrusions and mineral deposits (modified after maps provided by the Hubei Geological Bureau First Geological Brigade, 2005). QDOB: Qinling-Dabieshan Orogenic Belt, NCC: North China Craton, YC: Yangtze Craton. Area outlined in blue shows the location of the map in Fig. 2A.

2. Geological background

2.1. The Daye ore district

The Daye ore district is located in the westernmost part of the Middle-Lower Yangtze River Metallogenic Belt (Fig. 1A) and hosts one of the largest concentrations of Cu-Fe-Au skarn deposits in China, with minor porphyry Cu-Mo deposits (Pan and Dong, 1999; Li et al., 2014; Xie et al., 2015). The basement is dominated by Cambrian to Middle Triassic marine carbonates and clastic rocks and minor Late Triassic to Middle Jurassic clastic rocks (Fig. 1B; Shu et al., 1992). The most significant structures are Indosinian WNW- to NW-trending folds and numerous NNE faults which significantly controlled the emplacement of igneous intrusions and development of mineralization (Shu et al., 1992). The Daye ore district contains six major plutons (i.e., Echeng, Tieshan, Jinshidian, Lingxiang, Yangxin and Yinzhu, from north to south), with numerous associated porphyry stocks (Fig. 1B). The major plutons and stocks formed at 152 to 127 Ma (e.g., Li et al., 2009; Xie et al., 2011). According to Xie et al. (2013), magmatic-hydrothermal systems in the

Daye ore district can be classified into: (1) porphyry-style Cu-Mo-(W) and porphyry-related exoskarn-style Cu, Fe, Cu-Au, Cu-Fe-(Au), and Cu-Mo-W deposits (144–137 Ma), and associated porphyritic stocks comprising granites, granodiorites, quartz monzodiorites, quartz diorites and diorites (Suite 1: 147–136 Ma; Fig. 1B); and (2) exoskarn-style Fe deposits (133–120 Ma) and related granites, quartz diorites and diorites (Suite 2: 133–127 Ma; Fig. 1B).

2.2. The Tonglushan QMD porphyry-related skarn system

The Tonglushan QMD porphyry lies in the NW part of the Yangxin Pluton (Fig. 1B). It was mainly emplaced into Lower Triassic (dolomitic) limestone of the Daye Formation which is the main host for exoskarn-type Cu-Fe-(Au) mineralization (Shu et al., 1992). The main structures in the area are Indosinian NW-striking faults and folds (233–225 Ma) which are overprinted by younger Yanshanian NE-striking faults and folds (162–156 Ma; Wang, 2006). The intersections of these faults and folds provided the locus for the emplacement of the QMD porphyry as well as for associated fluid flow and mineralization (Shu et al., 1992).

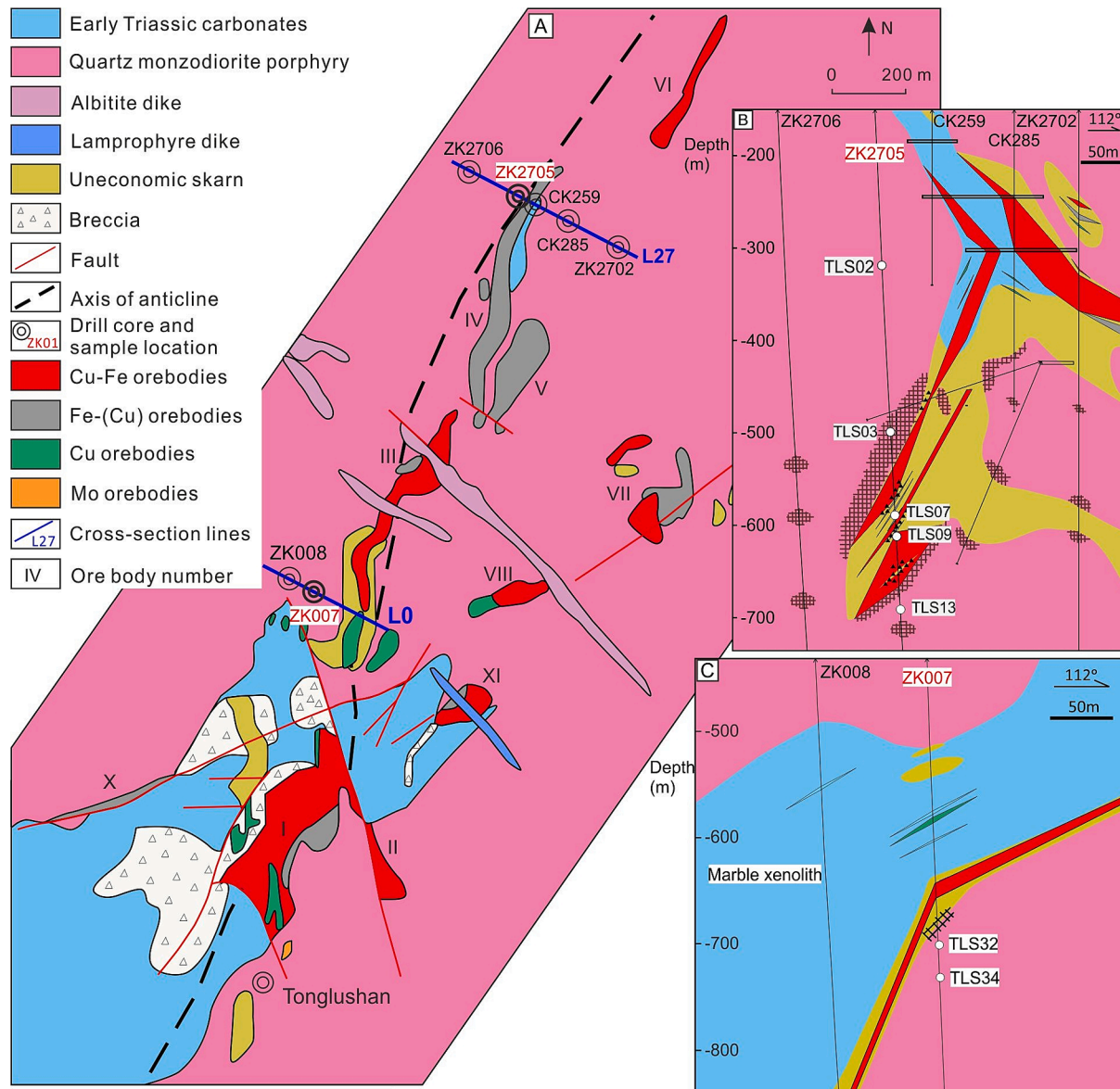


Fig. 2. (A) Simplified geological map of the Tonglushan Cu-Fe-(Au) deposit, showing the distribution of the main exposed Cu-Fe-(Au) orebodies. Note the hydrothermal breccias in the SW part of the area. Blue lines show the location of cross-sections in B and C. Cross-sections of (B) L27 and (C) L0 showing endo- and exoskarns, different types of ore bodies and sample locations (modified after the maps provided by the Hubei Geological Bureau First Geological Brigade).

Breccias, which are locally developed within carbonate xenoliths and wall rocks, mostly trend NE-SW (Fig. 2A).

The QMD is composed of 50–60 vol% plagioclase, 15–20 vol% K-feldspar, ~15 vol% hornblende, 10–15 vol% quartz, and <5 vol% biotite and ~3 vol% accessory minerals, mostly magnetite, titanite and apatite (Duan and Jiang, 2017; Zhang et al., 2021a). It is generally porphyritic with phenocrysts of plagioclase and amphibole with minor K-feldspar, quartz, and biotite. Its quartz and K-feldspar groundmass is generally fine-grained (0.3 to 0.5 mm), although grain size varies throughout the stock (Duan and Jiang, 2017; Zhang et al., 2021a). Previous petrogenetic studies indicated a crystallisation sequence from euhedral amphibole, plagioclase and apatite → subhedral-anhedral amphibole and plagioclase → biotite → quartz and K-feldspar (Duan and Jiang, 2017; Duan et al., 2021).

Hydrothermal alteration associated with the Tonglushan QMD porphyry is dominated by exoskarns in carbonate xenoliths and wall rocks, endoskarns within the intrusion, in proximity to surrounding carbonates, and weak potassic and sodic alteration and carbonatization further inside the stock (e.g., Zhao et al., 1990). The exoskarns, which contain most of the Cu-Fe mineralization (Fig. 2B, C), are mainly composed of diopside, garnet, epidote, phlogopite, amphibole, chlorite, and serpentine, with minor amounts of spinel, vesuvianite and scapolite. Abundant fine-grained aggregates of phlogopite replacing garnet and diopside, which are closely associated with copper and iron mineralization, are a particular characteristic of Tonglushan exoskarn deposits (Pan and Dong, 1999).

Endoskarn occurs as <100 m zones in the QMD porphyry up to its contacts with carbonate xenoliths and wall rocks (Fig. 2B). It is readily identifiable based on the presence of green diopside and brown garnet pseudomorphs after plagioclase and amphibole, and the presence of less-altered magmatic remnants. The endoskarns formed in five stages (Zhang et al., 2023): (1) muscovite-dominated; (2) prograde and (3)

retrograde skarnification; (4) potassic and (5) sodic alteration; and (6) carbonatization.

Potassic and sodic alteration is widespread in the pluton but is of weak intensity, preserving original igneous textures and most primary minerals. It is characterised by the presence of K-feldspar-(biotite)-quartz veins accompanied by local minor Fe-Cu sulfide mineralization. Later sodic alteration caused the replacement of plagioclase and K-feldspar by albite, chlorite and calcite, and amphibole and biotite with calcite, chlorite and titanite.

2.3. Samples and methods

All selected samples are from drill cores ZK2705 and ZK007 (Fig. 2B, C) and include relatively fresh QMD (TLS13 and TLS34; Fig. 3A) and potassic-sodic-altered QMD (TLS02 and TLS32; Fig. 3B), garnet-diopside-plagioclase endoskarn (TLS03; Fig. 3C), massive garnet exoskarn (TLS07; Fig. 3D) and Fe-(Cu) exoskarn (TLS09; Fig. 3E). Each sample was evaluated using optical microscopy, cold-cathodoluminescence (CL) and SEM-BSE imaging to characterise the abundance, shape, size, and internal texture of the apatite. Selected grains were analysed by EPMA and LA-ICP-MS to determine major and trace element compositions. All analyses were conducted at Camborne School of Mines, University of Exeter, UK.

CL imaging of apatite was carried out using a CITL Mk5 cold-cathode CL system operated with an accelerating voltage of approximately 8–12 kV and a current of 300–500 μ A. SEM-BSE imaging was undertaken using a Tescan VEGA 3 with an Oxford Instruments EDS spectrometer.

Electron microprobe analyses were performed using a JEOL JXA 8200 EPMA operated at 15 kV and 20 nA and with a beam diameter of 10 μ m. Analyses were carried out in areas free from inclusions or obvious defects and in specific zones of crystal growth or alteration as defined from CL imaging. Peak measurement times were 20 s for Ca and

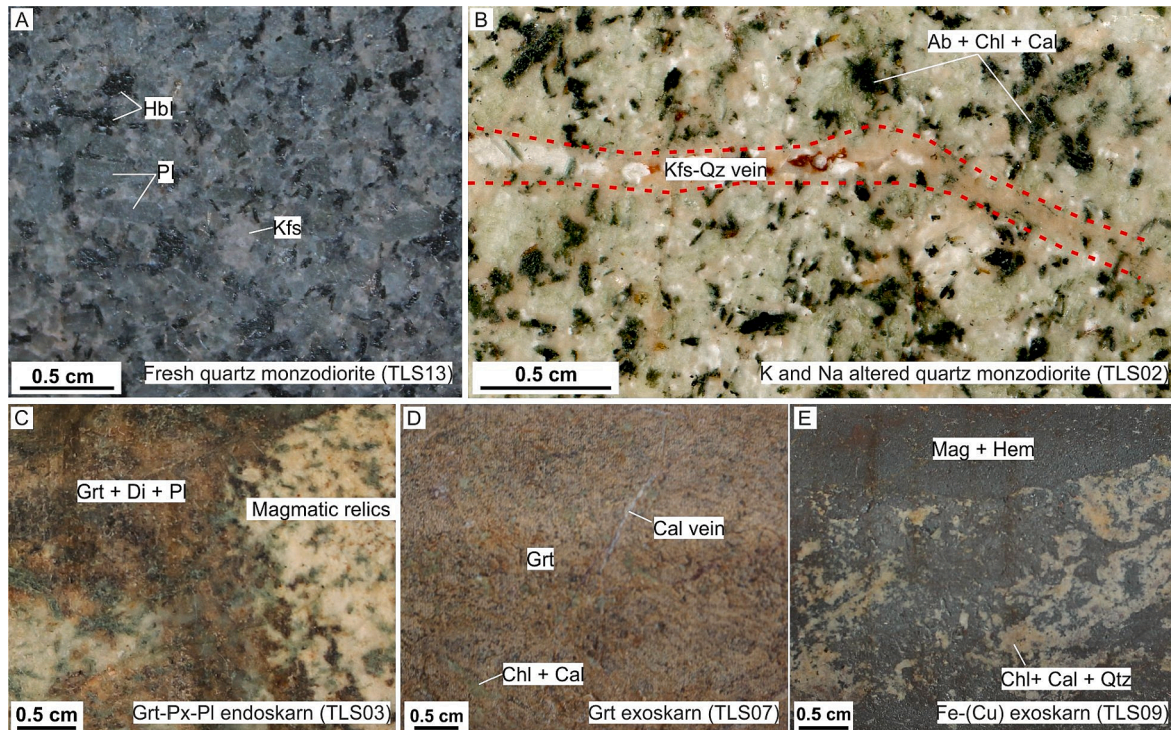


Fig. 3. Photographs of representative hand specimens. (A) Relatively fresh QMD with a porphyritic texture. (B) Potassic-sodic-altered QMD with potassic (Kfs + Qtz) and sodic (Ab + Chl + Cal) assemblages. (C) Endoskarn-altered QMD showing a prograde Grt + Di + Pl skarn and magmatic relics. (D) Massive garnet exoskarn partially replaced by retrograde chlorite + calcite assemblage, crosscut by a calcite vein. (E) Massive, disseminated Fe-(Cu) exoskarn showing Mag + Hem and Chl + Cal + Qtz assemblage. The prograde Grt + (Di) assemblage was wholly replaced as a result of retrograde alteration. Abbreviations: Ab = albite, Cal = calcite, Chl = chlorite, Di = diopside, Grt = garnet, Hbl = hornblende, Hem = hematite, Kfs = K-feldspar, Mag = magnetite, Pl = plagioclase, QMD = quartz monzodiorite, Qtz = quartz. Mineral abbreviations within in this paper follow the guidelines set out by Warr (2021).

P, 30 s for Fe and Mn, and 40 s for Na, Mg, Si, La, Ce, S, F and Cl. Background measurement times were half those of the peaks. The standards used were apatite (Ca, P, F), tugtupite (Cl), barite (S), orthoclase (Si), albite (Na), rhodonite (Mn), almandine (Fe), synthetic LaPO₄ (La) and synthetic REE-silicate (Ce). X-ray counts were converted to oxide concentrations using the Jeol $\phi\varphi z$ correction routine. To avoid issues with element diffusion under the electron beam (Stormer et al., 1993), preference was given to basal sections, the stage was continuously moved under a defocused beam, and F, Cl and Na were determined early in each analysis. Apatite formulae were calculated on the basis of 25 anions (O, OH, Cl and F) assuming ideal OH, with this estimated by difference assuming F + Cl + OH = 2, using the apatite stoichiometric model (Approach 2) of Ketcham (2015). For quality control purposes, data for individual analysis with wt.% totals (oxides plus F and Cl (corrected for O = F,Cl)) outside the range 97.5–101.5 wt% were disregarded.

LA-ICP-MS analysis was carried out using a New Wave Research 213 nm Nd-YAG laser coupled to an Agilent 7700 ICP-MS, within apatite grains that were previously analyzed by EPMA. Suitable areas for analysis, which were sufficiently homogeneous and inclusion-free, were common in apatite from the relatively fresh, potassic-sodic- and endoskarn-altered QMD, but there were only two such areas available in apatite from the exoskarns (see Electronic Supplementary Material; ESM_1). The laser was operated at 10 Hz with a 35 to 50 μm beam square and a fluence of approximately 4 J•cm⁻². The analysis time was 60 s, with a 30 s gas blank and 5 pulse pre-ablation. Measured mass numbers for each element are shown in ESM_2 Table 1. Median Ca concentrations in the apatite analysed, obtained by EPMA, were used for internal

calibration. NIST SRM 610 (Jochum et al., 2011) was analysed for external calibration. Repeat analyses of NIST 612 indicates <5% difference between certified values and average obtained values for Al, As, Sr, Mo, Ba, Pb, U, La, Ce, Pr, Sm, and Eu, 6 to 10% for Na, Mg, Si, Ti, Zn, Th, Nd, Gd, Tb and Ho, and 11 to 13% for Mn and the rest of the REE (see ESM_2 Fig. 1), while precision was better than 5% relative standard deviation for Na, Mg, Al, Si, V, and 6 to 10% for all other elements, except for Ti (11%) and Zn (13%).

3. Results

3.1. Apatite texture

Apatite in relatively fresh QMD (i.e., magmatic apatite) mostly forms euhedral crystals in the groundmass or mineral inclusions in plagioclase and hornblende which have long dimensions of 100 to 600 μm (Fig. 4A-C). Smaller grains (5 to 50 μm) locally occur as inclusions in plagioclase and magnetite. Apatite crystals in the relatively fresh QMD are homogeneous in transmitted light and BSE images (Fig. 4A) and typically have uniform yellow-green luminescence (Fig. 4B), although a few grains contain relatively dark green cores (Fig. 4C).

Apatite in QMD affected by potassic-sodic-alteration (i.e., with secondary K-feldspar + quartz + albite + chlorite + calcite), usually occurs in the groundmass or within phenocrysts such as plagioclase and hornblende. In transmitted light and SEM-BSE images it appears similar to apatite in fresh QMD (Fig. 4D, E). In CL images, however, it contains blue-green luminescent veins and patches and appears to have replaced magmatic yellow-green-luminescent apatite (Fig. 4F, G).

Table 1

Summary of mean values, and 1 σ from the mean, of analysed apatite obtained by EPMA in relatively fresh and potassic-sodic- and endoskarn-altered QMD, and exoskarns from the Tonglushan Cu-Fe-(Au) system.

Sample	Apatite in fresh QMD		Apatite in K-Na-altered QMD		Apatite in Grt-Px-Pl endoskarn		Apatite in Grt exoskarn		Apatite in Fe-(Cu) ores	
	TLS13, TLS34		TLS02, TLS32		TLS03		TLS07		TLS09	
	Mean	1 σ	Mean	1 σ	Mean	1 σ	Mean	1 σ	Mean	1 σ
(wt %)	n = 43		n = 23		n = 51		n = 41		n = 33	
CaO	53.8	0.44	54.0	0.44	54.2	0.45	56.0	0.42	55.7	0.44
Na ₂ O	0.12	0.06	0.07	0.02	0.07	0.04	0.02	0.02	0.04	0.02
MnO	0.08	0.04	0.06	0.03	0.04	0.03	0.02	0.02	0.04	0.03
MgO	0.01	0.01	0.00	0.00	0.01	0.03	0.01	0.03	0.00	0.00
FeO	0.08	0.09	0.05	0.03	0.08	0.06	0.28	0.22	0.30	0.23
La ₂ O ₃	0.22	0.09	0.23	0.09	0.18	0.10	0.12	0.07	0.16	0.09
Ce ₂ O ₃	0.26	0.09	0.29	0.10	0.22	0.08	0.22	0.09	0.35	0.13
P ₂ O ₅	41.5	0.57	41.6	0.48	41.6	0.53	40.8	0.90	41.1	0.81
SiO ₂	0.28	0.10	0.30	0.11	0.27	0.10	0.69	0.31	0.63	0.28
SO ₃	0.22	0.14	0.17	0.03	0.20	0.08	0.64	0.31	0.46	0.21
F	2.53	0.42	2.38	0.18	2.80	0.25	3.05	0.19	2.93	0.18
Cl	0.26	0.06	0.16	0.04	0.10	0.03	0.07	0.02	0.19	0.03
Total (uncorrected)	99.3	0.65	99.3	0.80	99.7	0.61	101.9	0.69	102.0	0.61
Total (corrected)	98.2	0.58	98.2	0.77	98.5	0.58	100.6	0.67	100.7	0.59
a.p.f.u.										
Ca	9.80	0.08	9.82	0.09	9.85	0.09	10.03	0.11	9.97	0.09
Na	0.038	0.018	0.022	0.007	0.022	0.015	0.007	0.006	0.012	0.006
Mn	0.012	0.005	0.008	0.004	0.006	0.005	0.003	0.003	0.005	0.004
Mg	0.001	0.003	0.001	0.001	0.001	0.008	0.002	0.007	0.000	0.001
Fe	0.012	0.013	0.007	0.004	0.011	0.009	0.039	0.031	0.043	0.032
La	0.014	0.005	0.015	0.006	0.011	0.006	0.007	0.004	0.010	0.006
Ce	0.016	0.005	0.018	0.006	0.014	0.005	0.013	0.005	0.022	0.008
P	5.97	0.05	5.97	0.03	5.97	0.04	5.77	0.10	5.82	0.08
Si	0.048	0.017	0.051	0.018	0.046	0.017	0.116	0.052	0.106	0.048
S	0.028	0.018	0.022	0.004	0.026	0.010	0.080	0.039	0.057	0.027
F	1.36	0.22	1.28	0.09	1.50	0.13	1.61	0.10	1.55	0.10
Cl	0.074	0.019	0.045	0.011	0.027	0.007	0.021	0.005	0.054	0.009
OH	0.567	0.223	0.676	0.096	0.472	0.135	0.369	0.105	0.399	0.093
X _{F-Ap}	0.68	0.11	0.64	0.05	0.75	0.07	0.81	0.05	0.77	0.05
X _{Cl-Ap}	0.04	0.01	0.02	0.01	0.01	0.00	0.01	0.00	0.03	0.00
X _{OH-Ap}	0.28	0.11	0.34	0.05	0.24	0.07	0.18	0.05	0.20	0.05

Note: Corrected total was calculated by subtracting half of the contribution from the halogens (F and Cl), corresponding to the surplus oxygen.

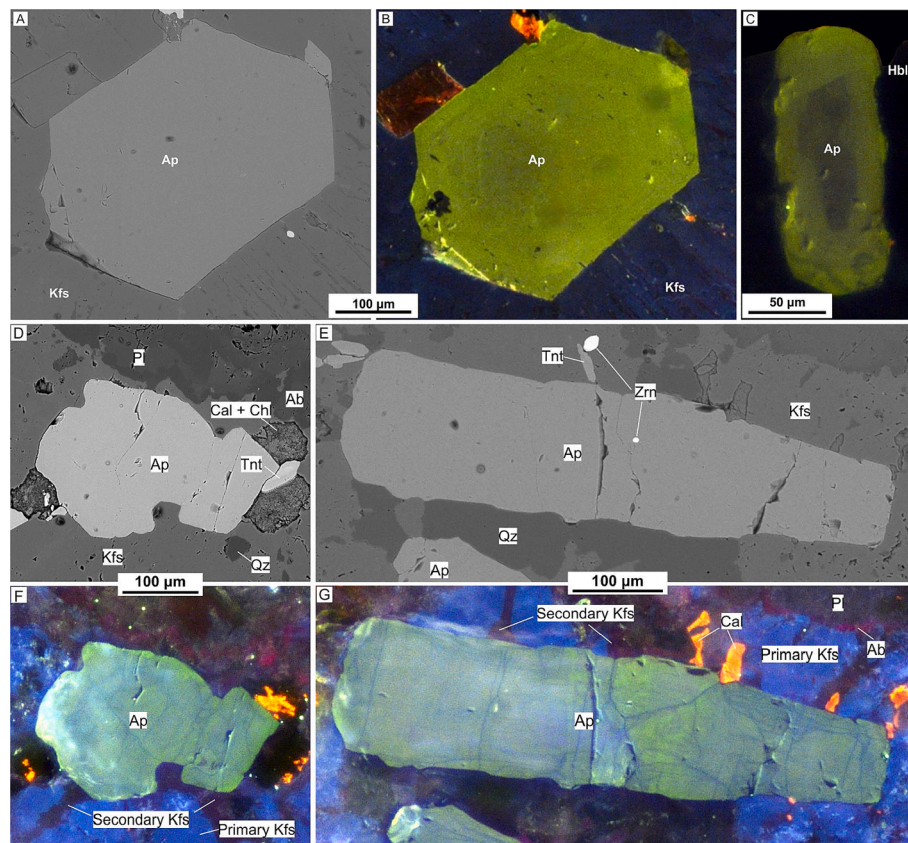


Fig. 4. SEM-BSE and CL images of apatite from (A-C) relatively fresh and (D-G) potassic-sodic-altered QMD. Apatite within a K-feldspar phenocryst in the relatively fresh host rock (TLS13) shows (A) euhedral and homogeneous textures and (B) sub-uniform yellow-green CL. (C) CL image of apatite crystal within a hornblende phenocryst in relatively fresh QMD (TLS13) showing yellow-green rim and dark green core. (D, E) Apatite from potassic-sodic-altered rock (TLS02) showing euhedral-subhedral and homogeneous textures in SEM-BSE images, but also (F, G) heterogeneous green luminescence overprinted and veined by blue and blue/green apatite. Abbreviations as per Fig. 3, plus Ap = apatite, Tnt = titanite.

Apatite in endoskarn usually occurs as discrete grains in the groundmass or as inclusions in garnet. It commonly occurs in the prograde skarn assemblage (i.e., garnet + diopside + plagioclase; Fig. 5A, B), and is generally subhedral-euhedral and 50–400 µm in diameter. It is homogeneous in SEM-BSE (Fig. 5A, B), similar to apatite in relatively fresh and potassic-sodic-altered QMD, but in CL shows mid-blue luminescent veins and replacements of igneous yellow-green apatite (Fig. 5C, D).

In garnet exoskarn, apatite in the prograde assemblage mainly occurs as inclusions in garnet and is generally subhedral-anhedral with navy blue-violet luminescence, with local pale yellow-green patches (Fig. 5E). Apatite associated with iron oxides (i.e., magnetite and hematite) in the Fe-(Cu) exoskarn shows bright blue luminescence with pale yellow-green patches (Fig. 5F).

3.2. Apatite composition

Apatite from the Tonglushan system is generally fluorapatite. In the relatively fresh QMD, it has relatively high Na₂O (0.12 ± 0.06 wt%), MnO (0.08 ± 0.04 wt%), FeO (0.08 ± 0.09 wt%), Cl (0.26 ± 0.06 wt%), Y (147 ± 31 ppm), and ΣREE (5310 ± 1018 ppm) compared to that in the altered QMD (Figs. 6–7; Tables 1–2). Endoskarn apatite has the lowest contents of MnO (0.04 ± 0.03 wt%), Mg (17.8 ± 13 ppm), Cl (0.10 ± 0.03 wt%) and highest F (2.77 ± 0.25 wt%), as well as slightly higher Sr/Y, La/Yb_N, La/Sm_N ratios, in comparison with apatite from the potassic- and sodic-altered rocks (Figs. 6–7; Tables 1–2). Exoskarn apatite has higher SiO₂ (0.63–0.69 wt%), SO₃ (0.46–0.64 wt%), and F (2.93–3.05 wt%), but lower Na₂O (0.02–0.04 wt%) and MnO (0.02–0.04 wt%) compared with that from the endoskarn (Fig. 6A–E; Table 1). It shows distinct trace element compositions compared to grains in relatively fresh or altered QMD (Fig. 7). In the garnet exoskarn it has low Sr (358 ± 12.0 ppm), Y (11.2 ± 0.21 ppm), V (9.01 ± 0.55 ppm), and high Ti (15.0 ± 1.48 ppm), As (222 ± 1.41 ppm), Pb (4.80 ±

0.57 ppm), Th (353 ± 39.6 ppm) and U (48.9 ± 1.63 ppm) (Fig. 7; Table 2). It has relatively MREE- and HREE-depleted patterns and moderately negative Eu/Eu* (Fig. 8; Table 2). Apatite in the Fe-(Cu) exoskarn has higher Cl than that in the garnet exoskarn (0.29 ± 0.03 wt % vs. 0.07 ± 0.02 wt%; Fig. 6E; Table 1). All apatite grains from the relatively fresh and altered QMD contain negligible Al, Cu, Zn, Mo, and Ba (typically below detection limits) and similar concentrations of Ti, V, As, Pb, Th and U (Table 2).

4. Discussion

4.1. Cause of variations in apatite luminescence

Apatite in the Tonglushan system can be classified into four basic varieties based on its colour in CL: (1) yellow-green luminescent apatite in relatively fresh QMD; (2) green-blue luminescent apatite in potassic-sodic-altered QMD; (3) distinct mid-blue luminescent apatite in the endoskarn; and (4) navy blue-violet to bright blue luminescent apatite in the exoskarn. Although CL spectra are not available for the apatite analysed here, some inferences about the CL activators can be made based on a comparison with published examples (Campbell and Henderson, 1997; Kempe and Götz, 2002; Bouzari et al., 2016; Cao et al., 2021):

Yellow-green CL in apatite from relatively fresh QMD is most likely due to relatively high concentrations of Mn²⁺, which is a common activator in apatite in felsic magmatic rocks (Marshall and Mariano, 1988; Kempe and Götz, 2002; Lisowiec et al., 2013). This inference is supported by the relatively high concentrations of Mn (581–1055 ppm; Fig. 7A–D) in the yellow-green-luminescent apatite.

Green-blue CL in apatite from the potassic-sodic-altered QMD is probably caused by relatively low Mn²⁺ (<430 ppm), as indicated by the trend of decreasing Mn from the yellow-green to green-blue luminescent apatite (Fig. 7A–D). From experimental studies, the green colour

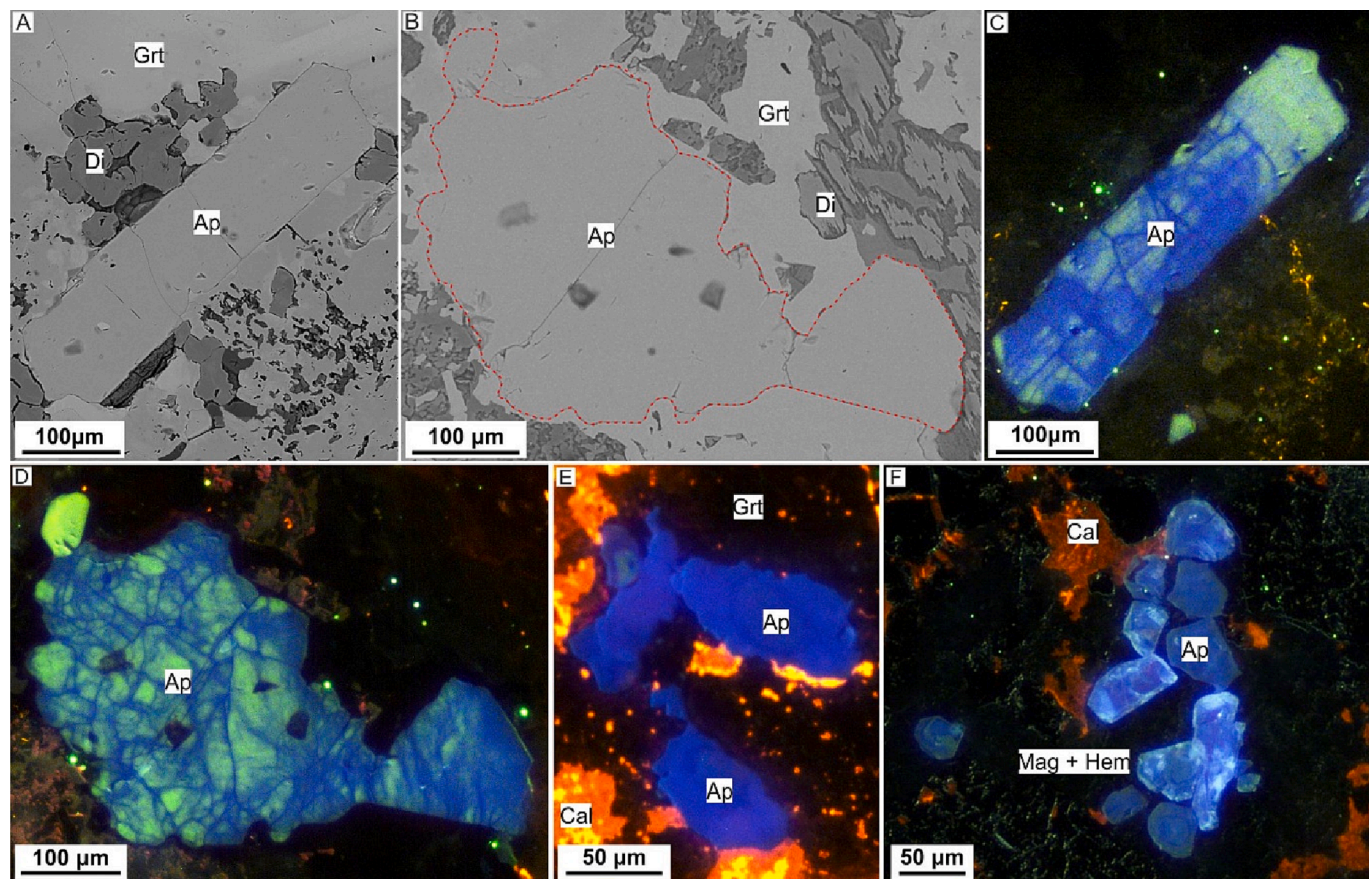


Fig. 5. SEM-BSE and CL images of apatite from the (A–D) endoskarn and (E, F) exoskarn in the Tonglushan system. Apatite associated with the prograde Grt + Di + Pl assemblage shows euhedral-subhedral and homogeneous textures in SEM-BSE images (A, B), and distinct mid-blue CL veins within and replacements of yellow-green-CL magmatic apatite (C, D). (E) Euhedral-subhedral navy blue-violet CL apatite associated with prograde skarn Grt assemblage in the garnet exoskarn. Some apatite grains have pale yellow-green-CL patches. (F) Euhedral-subhedral bright to dark blue CL apatite, with pale yellow-green CL patches, associated with Mag + Hem ores in the Fe-(Cu) exoskarn. Abbreviations as per Figs. 3 and 4.

could also be due to quenching of Mn²⁺-activated luminescence by Fe²⁺ (Filippelli and Delaney, 1993; Kempe and Götze, 2002), however this is unlikely here due to low concentrations of MnO (0.06 ± 0.03 wt%) and FeO (0.04 ± 0.03 wt%). More probable is that lower Mn reduced the dominance of the yellow emission in favour of colours induced by a variety of other activators, perhaps differing proportions of the REE.

In a similar way, but more intensively, the mid-blue, navy blue-violet to bright blue CL of apatite in the endoskarns and exoskarns also probably resulted from removal of Mn (Fig. 7A–D) and a more prominent signal from REE activators. Typical blue and lilac/violet CL in apatite from carbonatites is mainly caused by relatively high Ce³⁺, Eu²⁺ and Sm³⁺, and depletion in Mn (Kempe and Götze, 2002). Similar variations in apatite CL colours occur in the Matongo carbonatite phosphate deposit, Burundi, where apatite exhibits blue-green cores and blue-violet outer rims in CL, reflecting a change from Mn + REE to REE activation (Decréé et al., 2016).

The very strong violet blue- to bright blue-luminescence of apatite in the exoskarn is likely to be due to both low Mn (87.1 ± 6.51 ppm) (Fig. 7A–D) and low HREE (Fig. 8). As a result, the CL colour may be mainly controlled by the LREE. Waychunas (2002) showed that bright blue luminescence of apatite in exoskarns in the Bancroft and Wilberforce areas of Ontario is activated by Ce³⁺ and Eu²⁺. For the apatite in the Tonglushan exoskarn, this may work for Ce (1950 ± 10 ppm; Fig. 7D), which is slightly elevated compared with the other REE, but not for Eu which is depleted relative to levels in the relatively fresh and potassic-sodic- and endoskarn-altered QMD (Fig. 8).

4.2. Cause of variations in apatite chemistry

The trace element and halogen contents of apatite are likely to reflect the composition of the melt or fluid from which they crystallised, after accounting for any fluid-mineral and/or mineral–mineral element partitioning during crystallisation, or compositional features inherited from the protolith (Piccoli and Candela, 2002; Harlov, 2015). Studies of fluid-mineral interaction in experiments and naturally mineralised rocks show that the texture and chemistry of apatite can be modified by hydrothermal fluids with various salinities and acidity under a range of temperatures (<300–900 °C) and pressures (500–1000 MPa) (Harlov et al., 2002; 2005; 2007; Harlov and Forster, 2003).

In the Tonglushan QMD and its alteration products, apatite shows complex replacement textures in CL images indicating that it has undergone a number of episodes of modification during potassic-sodic- and endoskarn-alteration. In the relatively fresh QMD, subtle colour variations are interpreted to be due to variable metasomatic leaching of trace elements, specifically Mn, Na, Mg, Sr, Y, REE and Cl, which is in good agreement with experimental studies (Harlov et al., 2002; 2005; Harlov and Forster, 2003; Kusebauch et al., 2015) and observations of metasomatised natural samples from porphyry Cu systems (Bouzari et al., 2016; Cao et al., 2021). Among these components, Mn and Cl appear to be the most sensitive to metasomatic alteration. Apatite from the relatively fresh QMD has the highest Mn and Cl contents, with progressively lower concentrations in the potassic-sodic- and endoskarn-altered equivalents (Figs. 6 and 7). This results in the CL colour of the apatite changing from yellow-green in the relatively fresh QMD to green-blue in the potassic-sodic-altered rocks, to mid-blue in the endoskarns. A similar

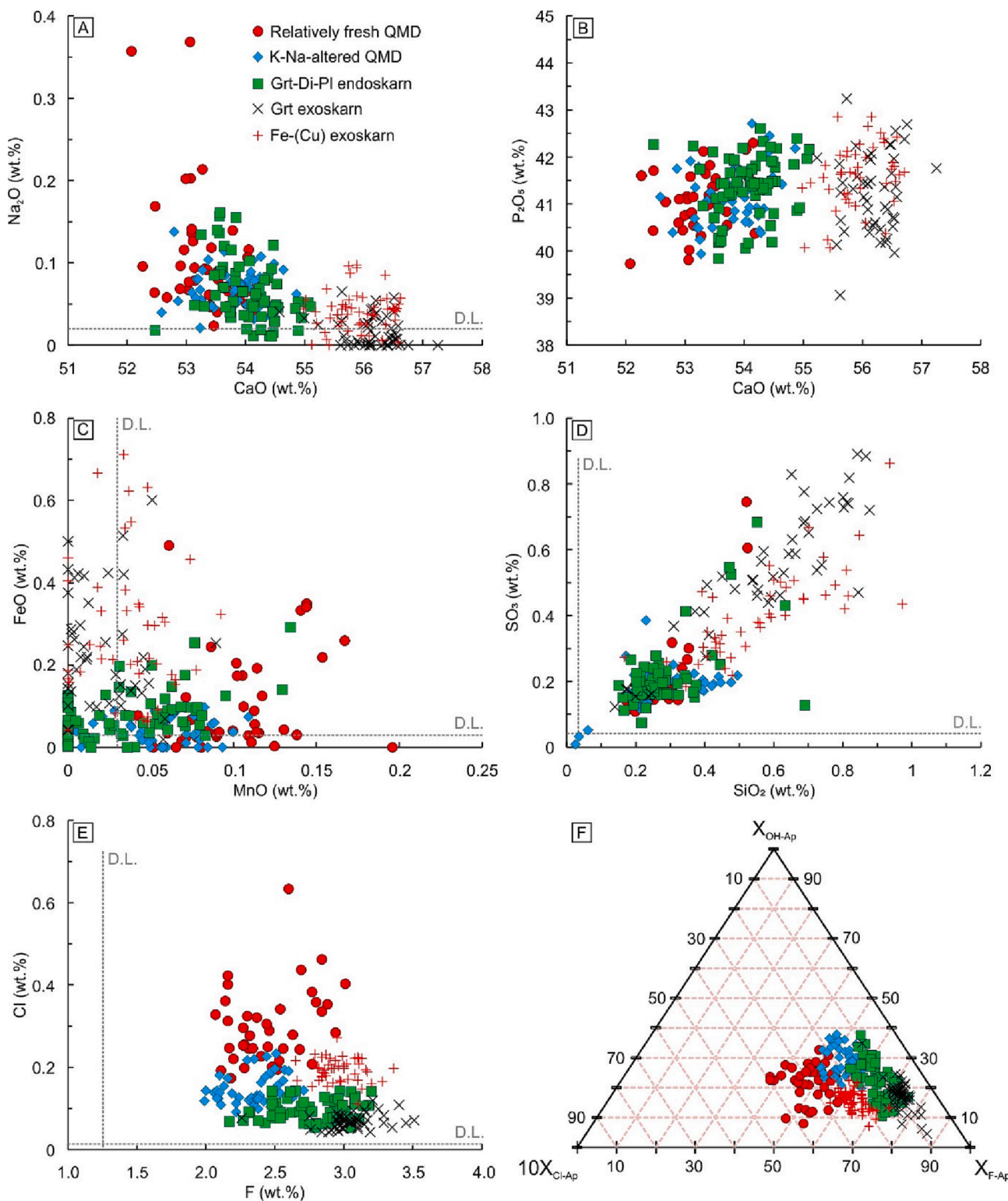


Fig. 6. Major element variations in apatite from the relatively fresh and potassic-sodic- and endoskarn-altered QMD and exoskarns. (A) CaO versus Na₂O; (B) CaO versus P₂O₅; (C) MnO versus FeO; (D) SiO₂ versus SO₃; (E) F versus Cl (wt.%); and (F) 10X_{Cl-Ap} versus X_{F-Ap} versus X_{OH-Ap} (mol%). Abbreviations as per Fig. 3, plus D. L. = detection limit.

colour change occurs in apatite in unaltered (yellow or brown), potassic (green) and phyllitic-altered (gray) rocks in several porphyry Cu deposits in British Columbia (Bouzari et al., 2016).

Variations in Mn, Sr and Mg in apatite involve substitutions in the Ca sites: Mn²⁺, Sr²⁺, Mg²⁺ ↔ Ca²⁺ (Pan and Fleet, 2002). Considering the positive correlation between Mn and both Sr and Mg (Fig. 7B, C), it is

likely that they replaced Ca during the same alteration process. Replacement of Ca²⁺ by Na⁺, as indicated by the negative correlation between Na₂O and CaO from the relatively fresh QMD to altered rocks (Fig. 6A), is possible via a number of coupled substitutions involving S⁶⁺, Si⁴⁺, P⁵⁺ and/or REE³⁺ (Ronsbo, 1989; Liu and Comodi, 1993; Tepper and Kuehner, 1999; Fleet et al., 2000; Parat et al., 2002)

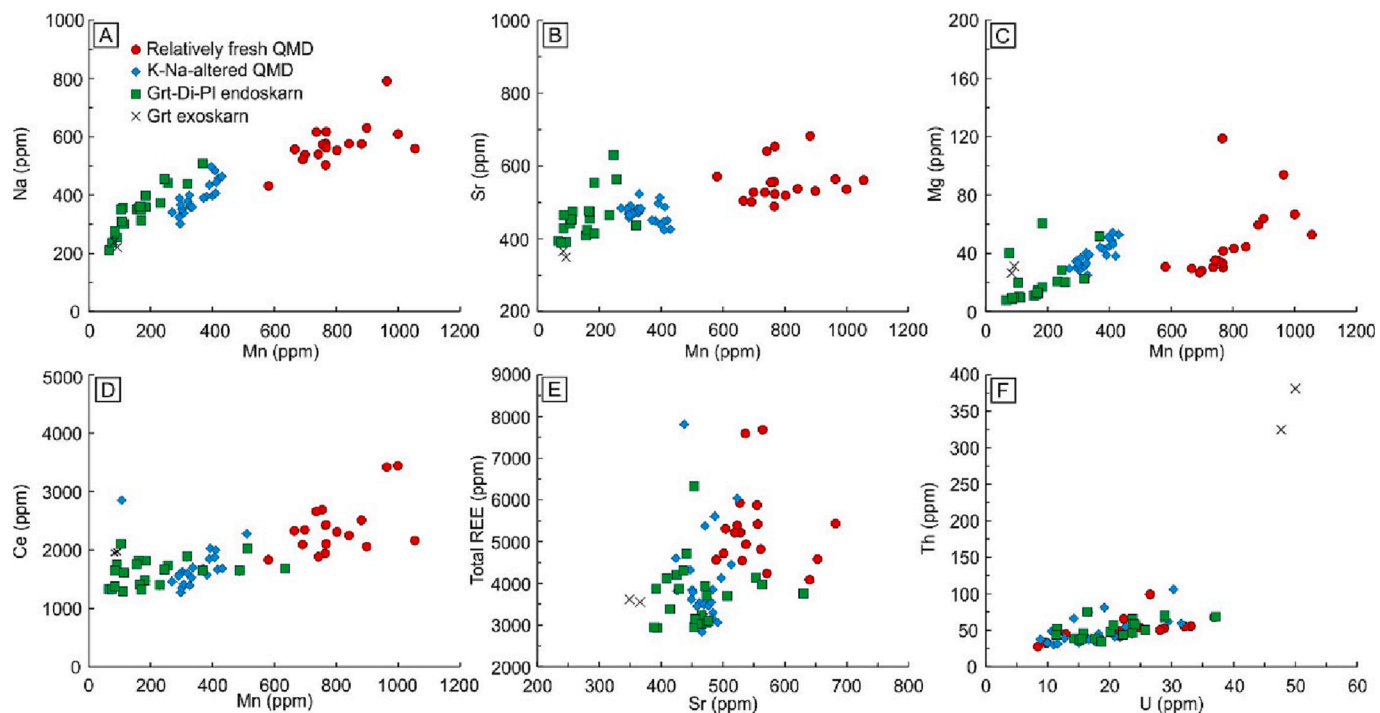
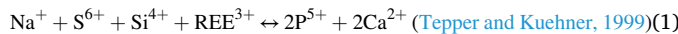


Fig. 7. Trace element variations in apatite from the relatively fresh and potassic-sodic- and endoskarn-altered QMD and exoskarn in the Tonglushan system. Abbreviations as per Fig. 3.

including:



Among these, reaction (1) provides the best explanation for the compositional variability of apatite (Fig. 9A). The absence of a positive correlation between Na and S (Fig. 9B), or Na and $\Sigma\text{REE} + \text{Y}$ (Fig. 9C) likely excludes the involvement of reactions (2) and (3). In addition, similar REE patterns for apatite in both relatively fresh and altered QMD (Fig. 8) indicates that the REE were not strongly depleted during metasomatism.

Apatite in the exoskarns is genetically associated with skarn minerals (e.g., garnet in the garnet exoskarn) and iron oxides (e.g., magnetite in the Fe-(Cu) exoskarn) and shows large compositional variations relative to apatite in the QMD porphyry. It has much higher contents of CaO, reflecting high Ca in the exoskarn protolith, consistent with apatite compositions observed in W skarns (Mao et al., 2016). Its major and trace element compositions, with high SO₃, As, and Pb, and low Mn, Na, Sr, Y, V and ΣREE , are likely to reflect introduction of SO₃, As, and Pb by the magmatic-hydrothermal fluids responsible for exoskarn formation and mineralisation.

4.3. Apatite as a tracer of endoskarns and porphyry-style alteration

Variations in the composition and texture of apatite in different rock types of the Tonglushan system are shown in Fig. 10. The extent of replacement as a result of apatite-fluid interaction is likely to be strongly related to the fluid/mineral ratio and composition of the metasomatic fluid. In general, a relatively more concentrated solution (i.e. for KOH, NaF and NaCl) and higher fluid/mineral ratio leads to more extensive replacement (Kusebauch et al., 2015). Apatite affected by porphyry-style potassic-sodic alteration shows modification along fractures and in patches (Fig. 4F), whereas endoskarn alteration caused pervasive changes, probably due to a higher fluid/mineral ratio. The metasomatic

fluids in both cases also removed Mn, Na, Cl, and to a lesser extent Mg, Sr, Y and REE, from the apatite (Fig. 6E and Fig. 7A-E).

The higher concentrations of F ($X_{\text{F-Ap}} = 0.74 \pm 0.07$) in apatite in the endoskarn compared with that in relatively fresh ($X_{\text{F-Ap}} = 0.67 \pm 0.07$) and potassic-sodic-altered ($X_{\text{F-Ap}} = 0.64 \pm 0.05$) QMD, suggests that the fluids causing endoskarn alteration were relatively F-rich (probably as HF), as suggested for the formation of the Empire Cu-Zn endoskarn, Idaho (Chang and Meinert, 2004), or that endoskarn formation released F into the fluids which then precipitated apatite locally.

In summary, apatite chemistry indicates that the fluids causing both endoskarn formation and potassic-sodic-style alteration of the QMD were rich in Na, Cl, Ca and F (Fig. 6A, E), with F facilitating the breakdown of silicates to enhance skarn formation.

4.4. Implications for mineral exploration

In recent years, the characteristics of apatite have been assessed as a potential indicator of magmatic systems capable of generating mineralisation (e.g., Duan and Jiang, 2018; Zhong et al., 2018; Sun et al., 2019; Pan et al., 2020) and for identifying specific types of deposits (Belousova et al., 2002; Cao et al., 2012; Mao et al., 2016; Pan et al., 2016; Rukhlov et al., 2016), mainly based on its unique chemical characteristics including REE and halogen contents. However, apatite can be variously altered by hydrothermal processes as revealed by complex textures in CL (Fig. 4 and Fig. 5). The modification of primary apatite, characterised by the apparent removal of certain trace elements (e.g., Mn, Na and Cl), can occur during almost all stages of alteration in a porphyry-related magmatic-hydrothermal system, i.e., from the higher temperatures of potassic- and endoskarn-alteration to lower temperatures of phyllitic and propylitic alteration. In addition, hydrothermal alteration can modify the Sr and O isotope compositions of apatite and so give misleading information on fluid sources (Zeng et al., 2016).

Cao et al. (2012) demonstrated that distinct concentrations and ratios of trace elements (e.g., Mn and REEs) in apatite can help discriminate several types of deposit, such as porphyry Cu-Mo, skarn Cu, Pb-Zn and Mo-W deposits. Using their Mn versus Sr discrimination diagram

Table 2

Summary of mean values, and 1σ from the mean, of analysed apatite obtained by LA-ICP-MS in relatively fresh, potassic-sodic- and endoskarn-altered QMD, and exoskarns from the Tonglushan Cu-Fe-(Au) system.

Sample	Apatite in fresh QMD		Apatite in K-Na-altered QMD		Apatite in Grt-Px-Pl endoskarn		Apatite in Grt exoskarn	
	TLS13 and TLS34		TLS02 and TLS32		TLS03		TLS07	
	Mean	1σ	Mean	1σ	Mean	1σ	Mean	1σ
(ppm)	n = 18		n = 24		n = 20		n = 2	
Na	574	71.5	389	51.2	338	67.8	230	13.8
Mg	48.0	25.0	38.6	8.08	17.8	12.9	28.8	3.32
Al	5.83	17.9	2.61	8.43	8.17	22.9	34.0	11.6
Si	1317	289	1354	339	1304	303	3250	56.6
Ti	8.73	2.67	10.1	1.23	8.92	2.34	15.0	1.48
V	14.1	2.4	17.3	7.71	15.5	4.37	9.01	0.55
Mn	799	122	347	50.3	154	68.9	87.1	6.51
Cu	0.47	0.22	1.75	1.12	0.84	0.64	1.49	1.23
Zn	1.09	2.31	0.49	0.23	0.4	0.21	2.55	0.21
As	16.3	4.74	12.8	4.76	25.5	11.7	222	1.41
Sr	554	53.3	470	24.6	460	61.1	358	12.0
Y	147	31.3	117	33.9	96.7	29.0	11.2	0.21
Mo	0.13	0.06	0.09	0.06	0.07	0.05	0.37	0.02
Ba	0.49	0.38	0.38	0.31	0.53	0.99	1.69	1.29
Pb	1.50	0.71	1.07	0.24	1.14	0.19	4.80	0.57
Th	49.7	16.5	48.2	18.6	52.3	12.2	353	39.6
U	21.5	8.62	18.0	6.27	20.6	6.70	48.9	1.63
La	2008	379	1572	419	1480	284	1145	49.5
Ce	2383	452	1810	507	1639	368	1960	14.1
Pr	173	32.5	130	38.6	116	30.5	143	2.26
Nd	556	112	419	125	374	109	301	7.78
Sm	67.5	13.8	51.1	16.2	45.1	14.9	17.0	2.33
Eu	12.6	2.48	10.1	3.20	8.41	2.47	3.26	0.33
Gd	50.1	11.1	40.4	12.3	35.6	11.2	10.3	1.91
Tb	5.10	1.16	4.01	1.24	3.47	1.28	0.81	0.13
Dy	24.7	5.48	19.6	6.08	16.5	5.46	3.31	0.98
Ho	4.69	1.05	3.85	1.13	3.24	1.15	0.53	0.07
Er	12.0	2.82	9.91	3.00	8.18	2.75	0.92	0.14
Tm	1.58	0.39	1.30	0.39	1.05	0.31	0.12	0.04
Yb	10.5	2.66	8.67	2.75	7.04	2.18	0.85	0.04
Lu	1.76	0.51	1.50	0.49	1.24	0.3	0.07	0.04
LREE	5250	1003	4033	1121	3698	820	3580	78.2
HREE	60.3	14.1	48.8	15.1	40.7	13.4	6.61	1.44
REE	5310	990	4083	1130	3739	814	3586	48
Ce/Ce*	0.95	0.02	0.94	0.02	0.93	0.02	1.13	0.01
Eu/Eu*	0.66	0.06	0.68	0.06	0.65	0.05	0.76	0.05
Sr/Y	3.92	0.86	4.27	0.93	5.02	1.13	32.1	0.47
La/Yb _N	133	23.6	124	7.43	147	22.1	915	1.27
La/Sm _N	19.1	3.29	19.7	1.73	21.3	2.94	43.1	7.77

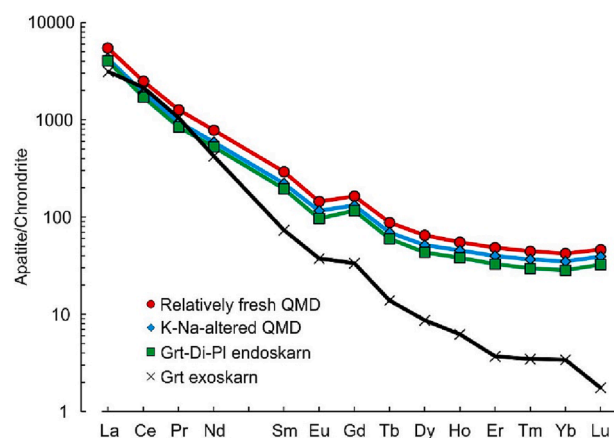


Fig. 8. Typical chondrite-normalised mean REE patterns for the relatively fresh and potassic-sodic- and endoskarn-altered QMD, and exoskarn in the Tonglushan system. Values for chondrite from McDonough and Sun (1995). Abbreviations as per Fig. 3.

(Fig. 11A), most apatite grains from relatively fresh and altered QMD in the Tonglushan system, as well as ore-related and ‘barren’ plutons in the Daye ore district, fall in the area for skarn Cu deposit. In contrast, in the plot of $(\text{La}/\text{Yb})_N$ versus Sr (Fig. 11B), most of them plot in the field for porphyry Cu-Mo deposits. Thus, these diagrams of single element concentrations or ratios in apatite may work for several types of deposit, such as Pb-Zn and Mo-W systems, but may not always be effective for discriminating porphyry and skarn deposits (Fig. 11A-B).

Mao et al. (2016) proposed discrimination diagrams based on apatite trace element data from a variety of ore deposit types (Fig. 11C-D). In Fig. 11C, apatite compositions from the relatively fresh QMD straddle the line dividing ‘barren’ rocks from those hosting ore deposits, whereas those from both the potassic-sodic-altered rocks and ‘barren’ endoskarns fall in the field for ore deposits. In Fig. 11D, apatite from the relatively fresh QMD mostly straddles the fields for porphyry-epithermal rocks and W skarns. However, most of the data for apatite from the potassic-sodic-altered QMD and endoskarns falls in the field for orogenic gold or $\text{Au} \pm \text{Co/Cu/Pb-Zn}$ skarns. This suggests that apatite chemistry alone is not an effective or accurate indicator of mineralization style.

As demonstrated in our study, a more reliable indicator is a combination of apatite CL colour (e.g., yellow-green, green-blue and blue), chemistry (mainly Mn, Na, Sr, Mg and Cl concentrations), and types of related hydrothermal alteration. Apatite CL colour is particularly indicative; Bouzari et al. (2016) found that it is possible to distinguish apatite from altered and unaltered rocks in several porphyry copper deposits in British Columbia based on its luminescence. Apatite luminesces green in K-altered rocks, whereas it shows a characteristic yellow/brown-luminescence in unaltered rocks. This could be applied in exploration, by investigating heavy minerals in regoliths and stream sediments. However, the use of apatite chemistry and CL still needs further testing, in a wider variety of case studies, to demonstrate consistent reliability where porphyry-related skarn systems vary considerably in their chemical and mineralogical characteristics.

5. Conclusions

- (1) Apatite from relatively fresh and potassic-sodic-altered QMD, endoskarns and exoskarns in the Tonglushan system show homogeneous textures but distinctive luminescence colours (yellow-green, green-blue, distinct mid-blue and navy blue-violet blue). This diversity is due to variations in the abundance and ratios of Mn and the REEs, such as Ce, which are primarily controlled by the composition of the protolith and metasomatic fluids.
- (2) The mid-blue luminescent apatite in endoskarn-altered rocks has relatively low Mn, Mg and Cl, and high Ca and F contents compared with apatite with green-blue luminescence in porphyry-style alteration. This suggests that mobilization of Mn, Mg and Cl during endoskarn formation was caused by fluids rich in Ca and F.
- (3) A combination of apatite CL colour and chemistry may provide a potential exploration indicator in porphyry- and endoskarn-exoskarn systems, providing that the apatite grains have not been significantly modified by post-crystallisation processes.

Declaration of Competing Interest

The authors declare the following financial interests/personal relationships which may be considered as potential competing interests:

Fei Zhang reports financial support was provided by China Scholarship Council. Sam Broom-Fendley reports financial support was provided by Natural Environment Research Council.

The remaining author declare that they have no known competing financial interests or personal relationships that could have appeared to influence the work reported in this paper.

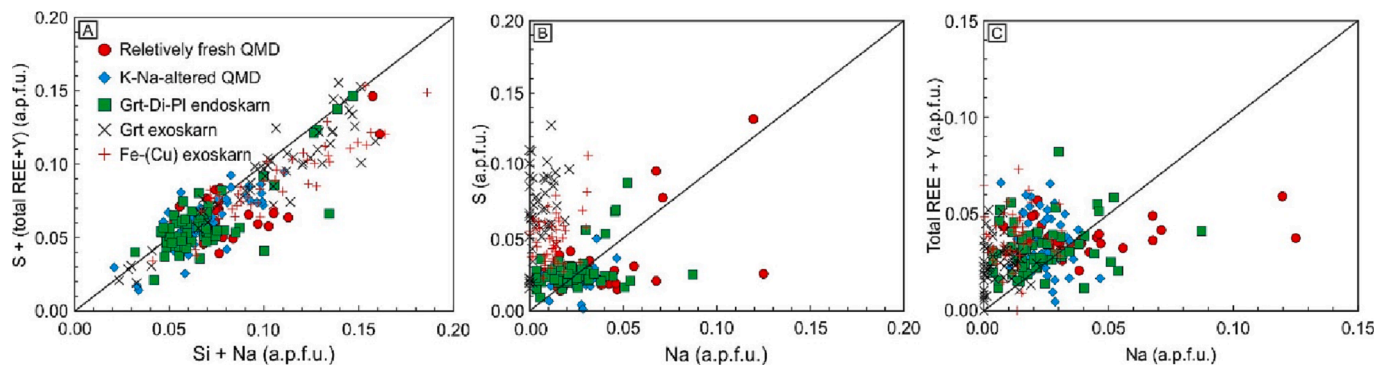


Fig. 9. Plots of (A) Si+Na versus S+(ΣREE+Y), (B) Na versus S, and (C) Na versus ΣREE+Y (a.p.f.u.) for apatite in the relatively fresh and altered QMD and endoskarn from the Tonglushan system. (A) The slope of the trend for $(S + (\Sigma\text{REE}+\text{Y})) / (\text{Si} + \text{Na})$ (a.p.f.u.) of ~1 is likely to be due to the substitution shown in reaction (1). Abbreviations as per Fig. 3.

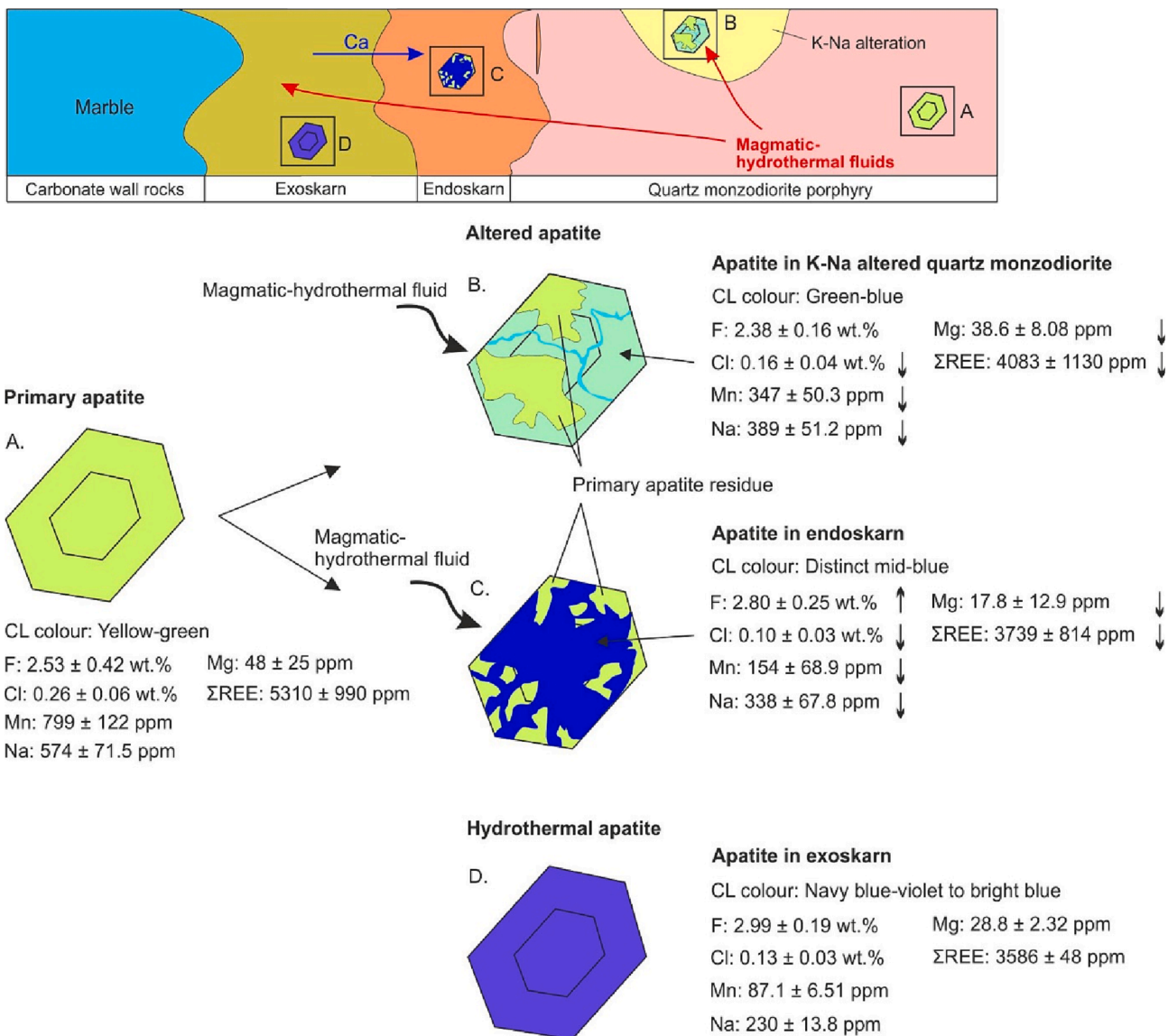


Fig. 10. Schematic figure illustrating the formation of magmatic and hydrothermal apatite in the relatively fresh-, potassic-sodic- and endoskarn-altered QMD, and exoskars in the Tonglushan system. (A) Magmatic, Mn-rich, yellow-green-luminescent apatite formed during the magmatic stage. (B) Magmatic yellow-green-luminescent apatite metasomatised during potassic-sodic alteration, reducing its Cl, Mn, Na, Mg and REE contents and changing its colour to green-blue. (C) Magmatic yellow-green-luminescent apatite metasomatised during endoskarn formation, resulting in a further decrease in Cl, Mn, Na, Mg and REE and a more pervasive and intense blue colour in CL. (D) Hydrothermal violet-blue- to bright blue-luminescent apatite, with the lowest contents of Cl, Mn, Na, Mg and REE among all types of apatite, crystallised as a result of exoskarn formation.

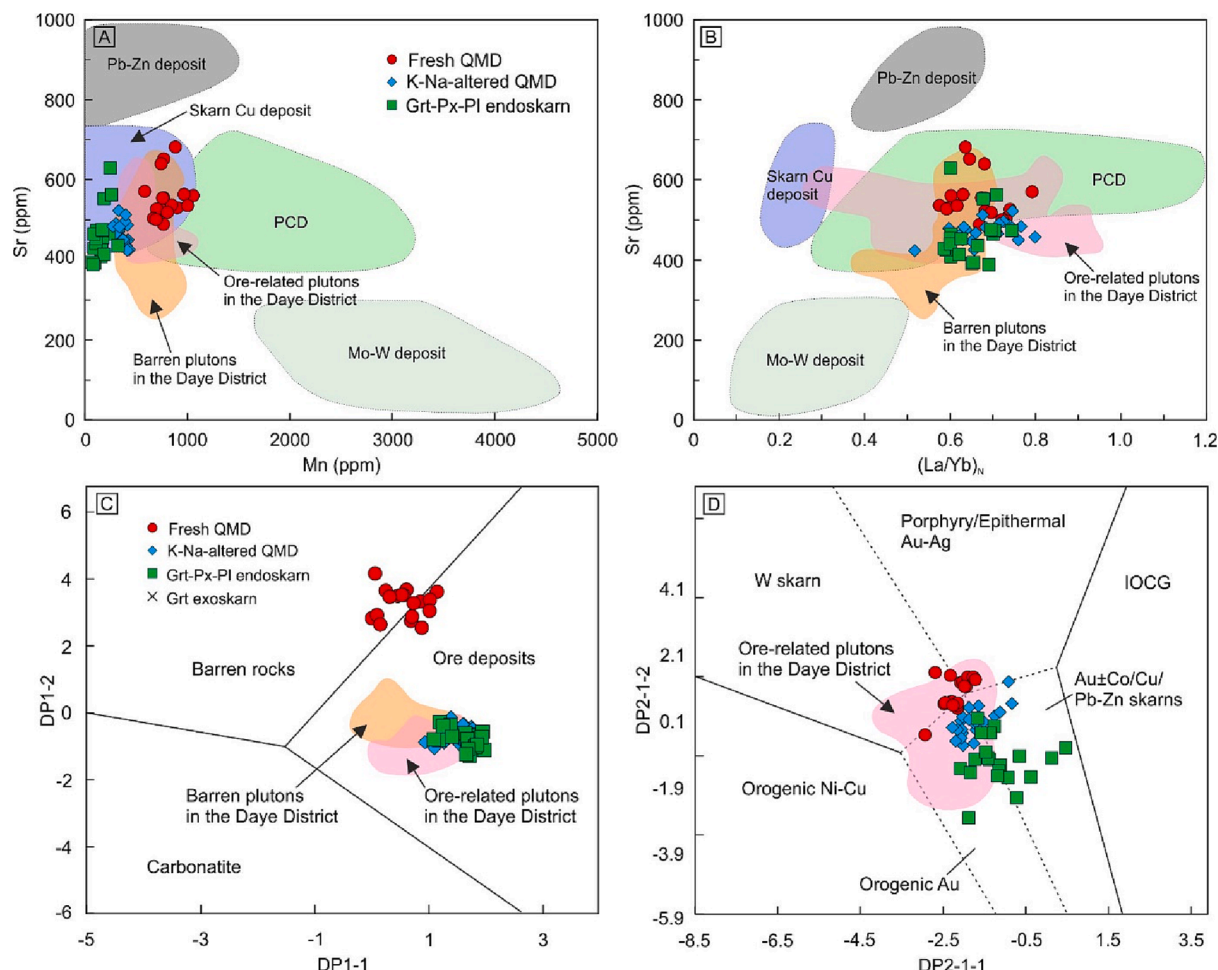


Fig. 11. Discrimination plots of (A) Mn (ppm) versus Sr (ppm) and (B) (La/Yb)_N versus Sr (ppm) for different types of deposit (after Cao et al., 2012). Discriminant projection plots for apatite composition: (C) DP1-1 versus DP1-2 and (D) DP2-1-1 versus DP2-1-2. Details for variables in C and D are described in Mao et al. (2016). The data for the apatite in the ore-related and ‘barren’ plutons are from Duan and Jiang (2018). Abbreviations as per Fig. 3.

Data availability

Data will be made available on request.

Acknowledgments

This research was financed by a China Scholarship Council and University of Exeter PhD Scholarship to FZ. SBF is funded by a Natural Environment Research Council (NERC) Industrial Innovation Fellowship (NE/R013403/1). The authors would like to thank Prof Jun Tan from China University of Geosciences (Wuhan), and geologists from the Geological Bureau First Geological Brigade for kindly providing assistance during fieldwork. D. Müller and an anonymous reviewer are gratefully acknowledged for comments on the manuscript.

Appendix A. Supplementary data

Supplementary data to this article can be found online at <https://doi.org/10.1016/j.oregeorev.2023.105493>.

References

- Andersson, S.S., Wagner, T., Jonsson, E., Fusswinkel, T., Whitehouse, M.J., 2019. Apatite as a tracer of the source, chemistry and evolution of ore-forming fluids: the case of the Olserum-Djupedal REE-phosphate mineralisation, SE Sweden. *Geochim. Cosmochim. Acta* 255, 163–187.
- Baele, J.M., Decrée, S., Rusk, B.G., 2019. Cathodoluminescence applied to ore geology and exploration. In: Decrée, S., Robb, L. (Eds.), *Ore deposits: Origin, exploration, and exploitation*. Wiley, New York, pp. 131–161.
- Bédard, É., Bronac, D.E., de Vazelhes, V., Beaudoin, G., 2022. Performance of predictive supervised classification models of trace elements in magnetite for mineral exploration. *J. Geochim. Explor.* 236, 106959.
- Belousova, E.A., Griffin, W.L., O'Reilly, S.Y., Fisher, N.I., 2002. Apatite as an indicator mineral for mineral exploration: Trace-element compositions and their relationship to host rock type. *J. Geochim. Explor.* 76 (1), 45–69.
- Bouzari, F., Hart, C.J.R., Bissig, T., Barker, S., 2016. Hydrothermal alteration revealed by apatite luminescence and chemistry: a potential indicator mineral for exploring covered porphyry copper deposits. *Econ. Geol.* 111 (6), 1397–1410.
- Boyce, J.W., Hervig, R.L., 2009. Apatite as a monitor of late-stage magmatic processes at Volcán Irazú, Costa Rica. *Contrib. Mineral. Petro.* 157 (2), 135–145.
- Bromiley, G.D., 2021. Do concentrations of Mn, Eu and Ce in apatite reliably record oxygen fugacity in magmas? *Lithos* 384–385, 105900.
- Broom-Fendley, S., Styles, M.T., Appleton, J.D., Gunn, G., Wall, F., 2016. Evidence for dissolution-reprecipitation of apatite and preferential LREE mobility in carbonatite-derived late-stage hydrothermal processes. *Am. Mineral.* 101 (3), 596–611.
- Broom-Fendley, S., Siegfried, P.R., Wall, F., O'Neill, M., Brooker, R.A., Fallon, E.K., Pickles, J.R., Banks, D.A., 2021. The origin and composition of carbonatite-derived carbonate-bearing fluorapatite deposits. *Miner. Deposita* 56 (5), 863–884.
- Brugge, E., Wilkinson, J.J., Miles, A., 2017. Habit and Chemistry of Apatite at Chuquicamata, Chile: 15th Biennial Society for Geology Applied to Mineral Deposits (SGA) Conference. Proceedings, Quebec City, 287–290.
- Campbell, L.S., Henderson, P., 1997. Apatite paragenesis in the Bayan Obo REE-Nb-Fe ore deposit, China. *Lithos* 42, 89–103.
- Cao, M.J., Li, G.M., Qin, K.Z., Seitmuratova, E.Y., Liu, Y.S., 2012. Major and trace element characteristics of apatites in granitoids from central Kazakhstan: implications for petrogenesis and mineralization. *Resour. Geol.* 62, 63–83.
- Cao, M.J., Evans, N.J., Hollings, P., Cooke, D.R., McInnes, B.I.A., Qin, K.Z., 2021. Apatite texture, composition, and O-Sr-Nd isotope signatures record magmatic and hydrothermal fluid characteristics at the Black Mountain porphyry deposit, Philippines. *Econ. Geol.* 116, 1189–1207.

- Chakhmouradian, A.R., Reguir, E.P., Zaitsev, A.N., Couëslan, C., Xu, C., Kynický, J., Mumin, A.H., Yang, P., 2017. Apatite in carbonatitic rocks: compositional variation, zoning, element partitioning and petrogenetic significance. *Lithos* 274–275, 188–213.
- Chang, Z., Meinert, L.D., 2004. The magmatic-hydrothermal transition - Evidence from quartz phenocryst textures and endoskarn abundance in Cu-Zn skarns at the Empire Mine, Idaho, USA. *Chem. Geol.* 210 (1-4), 149–171.
- Chang, Z.S., Mrozek, S.A., Meinert, L.D., Windle, S., 2015. Skarn-porphyry transition - an example from the Antamina skarn, Peru. In: ACRIM 2015 Congress. Australasian Institute of Mining and Metallurgy (AusIMM), Hong Kong, pp. 409–413.
- Cooke, D.R., Agnew, P., Hollings, P., Baker, M., Chang, Z., 2017. Porphyry indicator minerals (PIMS) and porphyry vectoring and fertility tools (PVFTS) – Indicators of mineralization styles and recorders of hypogene geochemical dispersion halos. Sixth Decennial International Conference on Mineral Exploration, 457–470.
- Decree, S., Boulvais, P., Tack, L., André, L., Baele, J.-M., 2016. Fluorapatite in carbonatite-related phosphate deposits: the case of the Matongo carbonatite (Burundi). *Miner. Deposita* 51 (4), 453–466.
- Decré, S., Cawthorn, G., Deloule, E., Mercadier, J., Frimmel, H., Baele, J.M., 2020. Unravelling the processes controlling apatite formation in the Phalaborwa Complex (South Africa) based on combined cathodoluminescence, LA-ICPMS and in-situ O and Sr isotope analyses. *Contrib. Mineral. Petro.* 175, 1–31.
- Duan, D.F., Jiang, S.Y., 2017. In situ major and trace element analysis of amphiboles in quartz monzodiorite porphyry from the Tonglshan Cu-Fe-(Au) deposit, Hubei Province, China: insights into magma evolution and related mineralization. *Contrib. Miner. Petro.* 172, 1–17.
- Duan, D.F., Jiang, S.Y., 2018. Using apatite to discriminate synchronous ore-associated and barren granitoid rocks: a case study from the Edong metallogenic district, South China. *Lithos* 310–311, 369–380.
- Duan, D.-F., Jiang, S.-Y., Tang, Y.-J., Wu, Y., Zhou, B., Zhu, J., 2021. Chlorine and sulfur evolution in magmatic rocks: a record from amphibole and apatite in the Tonglshan Cu-Fe (Au) skarn deposit in Hubei Province, south China. *Ore Geol. Rev.* 137, 104312.
- Dupuis, C., Beaudoin, G., 2011. Discriminant diagrams for iron oxide trace element fingerprinting of mineral deposit types. *Miner. Deposita* 46 (4), 319–335.
- Economos, R., Boehnke, P., Burgisser, A., 2017. Sulfur isotopic zoning in apatite crystals: a new record of dynamic sulfur behavior in magmas. *Geochim. Cosmochim. Acta* 215, 387–403.
- Einaudi, M.T., Burt, D.M., 1982. Introduction-terminology, classification, and composition of skarn deposits. *Econ. Geol.* 77, 745–754.
- Filippelli, G.M., Delaney, M.L., 1993. The effect of manganese (II) and iron (II) on the cathodoluminescence signal in synthetic apatite. *J. Sediment. Res.* 63, 167–173.
- Fleet, M.E., Liu, X., Pan, Y., 2000. Site preference of rare earth elements in hydroxyapatite $[Ca_{10}(PO_4)_6(OH)_2]$. *J. Solid State Chem.* 149 (2), 391–398.
- Harlov, D.E., 2015. Apatite: a fingerprint for metasomatic processes. *Elements* 11 (3), 171–176.
- Harlov, D.E., Forster, H.-J., 2003. Fluid-induced nucleation of (Y+REE)-phosphate minerals within apatite: nature and experiment. Part II. Fluorapatite. *Am. Mineral.* 88 (8-9), 1209–1229.
- Harlov, D.E., Förster, H.-J., Nijland, T.G., 2002. Fluid-induced nucleation of (Y+REE)-phosphate minerals within apatite: nature and experiment. Part I. Chlorapatite. *Am. Mineral.* 87 (2-3), 245–261.
- Harlov, D.E., Wirth, R., Förster, H.-J., 2005. An experimental study of dissolution-reprecipitation in fluorapatite: fluid infiltration and the formation of monazite. *Contrib. Mineral. Petro.* 150 (3), 268–286.
- Harlov, D.E., Marschall, H.R., Hanel, M., 2007. Fluorapatite-monazite relationships in granulite-facies metapelites, Schwarzwald, southwest Germany. *Mineral. Mag.* 71 (2), 223–234.
- Harlov, D.E., Meighan, C.J., Kerr, I.D., Samson, I.M., 2016. Mineralogy, chemistry, and fluid-aided evolution of the pea ridge Fe oxide-(Y+REE) deposit, Southeast Missouri, USA. *Econ. Geol.* 111 (8), 1963–1984.
- Huang, X.W., Sappin, A.A., Boutroy, E., Beaudoin, G., Makvandi, S., 2019. Trace element composition of igneous and hydrothermal magnetite from porphyry deposits: relationship to deposit subtypes and magmatic affinity. *Econ. Geol.* 114, 917–952.
- Jochum, K.P., Weis, U., Stoll, B., Kuzmin, D., Yang, Q., Raczek, I., Jacob, D.E., Stracke, A., Birbaum, K., Frick, D.A., Günther, D., Enzweiler, J., 2011. Determination of reference values for NIST SRM 610–617 glasses following ISO guidelines. *Geostand. Geoanal. Res.* 35, 397–429.
- Kempe, U., Götz, J., 2002. Cathodoluminescence (CL) behaviour and crystal chemistry of apatite from rare-metal deposits. *Mineral. Mag.* 66 (1), 151–172.
- Ketcham, R.A., 2015. Technical Note: Calculation of stoichiometry from EMP data for apatite and other phases with mixing on monovalent anion sites. *Am. Mineral.* 100 (7), 1620–1623.
- Konecke, B.A., Fiege, A., Simon, A.C., Parat, F., Stechern, A., 2017. Co-variability of S^{6+} , S^{4+} , and S^{2-} in apatite as a function of oxidation state: Implications for a new oxybarometer. *Am. Mineral.* 102 (3), 548–557.
- Kusebauch, C., John, T., Whitehouse, M.J., Klemme, S., Putnis, A., 2015. Distribution of halogens between fluid and apatite during fluid-mediated replacement processes. *Geochim. Cosmochim. Acta* 170, 225–246.
- Lee, R.G., Byrne, K., D'Angelo, M., Hart, C.J.R., Hollings, P., Gleeson, S.A., Alfaro, M., 2021. Using zircon trace element composition to assess porphyry copper potential of the Guichon Creek batholith and Highland Valley Copper deposit, south-central British Columbia. *Miner. Deposita* 56 (2), 215–238.
- Li, J.W., Vasconcelos, P.M., Zhou, M.F., Deng, X.D., Cohen, B., Bi, S.J., Zhao, X.F., Selby, D., 2014. Longevity of magmatic-hydrothermal systems in the Daye Cu-Fe-Au District, eastern China with implications for mineral exploration. *Ore Geol. Rev.* 57, 375–392.
- Li, J.-W., Zhao, X.-F., Zhou, M.-F., Ma, C.-Q., de Souza, Z.S., Vasconcelos, P., 2009. Late Mesozoic magmatism from the Daye region, eastern China: U-Pb ages, petrogenesis, and geodynamic implications. *Contrib. Mineral. Petro.* 157 (3), 383–409.
- Lisowiec, K., Slaby, E., Gotze, J., 2013. Cathodoluminescence (CL) of apatite as an insight into magma mixing in the granitoid pluton of Karkonosze, Poland. Conference on Raman and Luminescence Spectroscopy in the Earth Sciences, Vienna, 67–68.
- Liu, Y., Comodi, P., 1993. Some aspects of the crystal-chemistry of apatites. *Mineral. Mag.* 57 (389), 709–719.
- Loader, M.A., Wilkinson, J.J., Armstrong, R.N., 2017. The effect of titanite crystallisation on Eu and Ce anomalies in zircon and its implications for the assessment of porphyry Cu deposit fertility. *Earth Planet. Sci. Lett.* 472, 107–119.
- Lu, J., Chen, W., Ying, Y., Jiang, S., Zhao, K., 2021. Apatite texture and trace element chemistry of carbonatite-related REE deposits in China: implications for petrogenesis. *Lithos* 398–399, 106276.
- Lu, Y.J., Loucks, R.R., Fiorentini, M., McCuaig, T.C., Evans, N.J., Yang, Z.M., Hou, Z.Q., Kirkland, C.L., Parra-avila, L.A., Kobussen, A., 2016. Zircon compositions as a pathfinder for porphyry Cu ± Mo ± Au deposits. *Econ. Geol.* 19, 329–347.
- Mao, M., Rukhlov, A.S., Rowins, S.M., Spence, J., Coogan, L.A., 2016. Apatite trace element compositions: a robust new tool for mineral exploration. *Econ. Geol.* 111 (5), 1187–1222.
- Marshall, D.J., Mariano, A.N., 1988. Some further geological applications of cathodoluminescence. In: Marshall, D.J. (Ed.), Cathodoluminescence of geological materials. Unwin Hyman, Boston, pp. 94–124.
- Meinert, L.D., Dippe, G.M., Niculescu, S., 2005. World Skarn deposits. *Econ. Geol.* 100th Anniversary Volume 299–336.
- Mercer, C.N., Watts, K.E., Gross, J., 2020. Apatite trace element geochemistry and cathodoluminescent textures—A comparison between regional magmatism and the Pea Ridge IOAREE and Boss IOCG deposits, southeastern Missouri iron metallogenic province, USA. *Ore Geol. Rev.* 116, 103129.
- Miles, A.J., Graham, C.M., Hawkesworth, C.J., Gillespie, M.R., Hinton, R.W., Bromiley, G.D., 2014. Apatite: a new redox proxy for silicic magmas? *Geochim. Cosmochim. Acta* 132, 101–119.
- Nathwani, C.L., Loader, M.A., Wilkinson, J.J., Buret, Y., Sievwright, R.H., Hollings, P., 2020. Multi-stage arc magma evolution recorded by apatite in volcanic rocks. *Geology* 48, 323–327.
- Pacey, A., Wilkinson, J.J., Cooke, D.R., 2020. Chlorite and epidote mineral chemistry in porphyry ore systems: a case study of the northparkes district, New South Wales, Australia. *Econ. Geol.* 115, 701–727.
- Palma, G., Barra, F., Reich, M., Valencia, V., Simon, A.C., Vervoort, J., Leisen, M., Romero, R., 2019. Halogens, trace element concentrations, and Sr-Nd isotopes in apatite from iron oxide-apatite (IOA) deposits in the Chilean iron belt: evidence for magmatic and hydrothermal stages of mineralization. *Geochim. Cosmochim. Acta* 246, 515–540.
- Pan, Y., Dong, P., 1999. The Lower Changjiang (Yangzi/Yangtze River) metallogenic belt, east central China: intrusion- and wall rock-hosted Cu-Fe-Au, Mo, Zn, Pb, Ag deposits. *Ore Geol. Rev.* 15 (4), 177–242.
- Pan, Y., Fleet, M.E., 2002. Compositions of the apatite-group minerals: Substitution mechanisms and controlling factors. *Rev. Mineral. Geochem.* 48 (1), 13–49.
- Pan, L.C., Hu, R.Z., Wang, X.S., Bi, X.W., Zhu, J.J., Li, C.S., 2016. Apatite trace element and halogen compositions as petrogenetic-metallocgenic indicators: examples from four granite plutons in the Sanjiang region, SW China. *Lithos* 254–255, 118–130.
- Pan, L.-C., Hu, R.-Z., Bi, X.-W., Wang, Y., Yan, J., 2020. Evaluating magmatic fertility of Paleo-Tethyan granitoids in eastern Tibet using apatite chemical composition and Nd isotope. *Ore Geol. Rev.* 127, 103757.
- Parat, F., Dungan, M.A., Streck, M.J., 2002. Anhydrite, pyrrhotite, and sulfur-rich apatite: tracing the sulfur evolution of an Oligocene andesite (Eagle Mountain, CO, USA). *Lithos* 64 (3-4), 63–75.
- Piccoli, P.M., Candela, P.A., 2002. Apatite in igneous systems. *Rev. Mineral. Geochem.* 48 (1), 255–292.
- Qu, P., Yang, W., Niu, H., Li, N., Wu, D., 2022. Apatite fingerprints on the magmatic-hydrothermal evolution of the Daheishan giant porphyry Mo deposit, NE China. *Geol. Soc. Am. Bull.* 134 (7–8), 1863–1876.
- Ronso, J.G., 1989. Coupled substitutions involving REEs and Na and Si in apatites in alkaline rocks from the Ilmaussaq intrusion, South Greenland, and the petrological implications. *Am. Mineral.* 74, 896–901.
- Roy-Garand, A., 2019. Characterization of apatite within the Mactung W (Cu, Au) skarn deposit, Northwest Territories: implication for the evolution of skarn fluids. Saint Mary's University, 1–89.
- Rukhlov, A.S., Plouffe, A., Ferbey, T., Mao, M., Spence, J., 2016. Application of trace-element compositions of detrital apatite to explore for porphyry deposits in central British Columbia. *Geol. Fieldwork* 2015, 145–179.
- Shu, Q.A., Chen, P.R., Chen, J.R., 1992. *Geology of Fe-Cu Ore Deposits in Eastern Hubei Province*. Press of Metallurgical Industry, Beijing, p. 510.
- Stormer, J., Pierson, M., Tacker, R., 1993. Variation of F and Cl X-ray intensity due to anisotropic diffusion in apatite. *Am. Mineral.* 78, 641–648.
- Streck, M.J., Dilles, J.H., 1998. Sulfur evolution of oxidized arc magmas as recorded in apatite from a porphyry copper batholith. *Geology* 26, 523–526.
- Sun, S.J., Yang, X.Y., Wang, G.J., Sun, W.D., Zhang, H., Li, C.Y., Ding, X., 2019. In situ elemental and Sr-O isotopic studies on apatite from the Xu-Huai intrusion at the southern margin of the North China Craton: Implications for petrogenesis and metallogeny. *Chem. Geol.* 510, 200–214.
- Tepper, J.H., Kuehner, S.M., 1999. Complex zoning in apatite from the Idaho batholith: a record of magma mixing and intracrystalline trace element diffusion. *Am. Mineral.* 84 (4), 581–595.
- Wang, Y., 2006. The onset of the Tan-Lu fault movement in eastern China: Constraints from zircon (SHRIMP) and $^{40}\text{Ar}/^{39}\text{Ar}$ dating. *Terra Nova*, 18, 423–431.

- Warr, L.N., 2021. IMA–CNMNC approved mineral symbols. *Mineral. Mag.* 85 (3), 291–320.
- Waychunas, G.A., 2002. Apatite luminescence. *Rev. Mineral. Geochem.* 48, 701–748.
- Webster, J.D., Piccoli, P.M., 2015. Magmatic apatite: a powerful, yet deceptive, mineral. *Elements* 11 (3), 177–182.
- Wilkinson, J.J., Chang, Z.S., Cooke, D.R., Baker, M.J., Wilkinson, C.C., Inglis, S., Chen, H.Y., Bruce Gemmell, J., 2015. The chlorite proximitor: a new tool for detecting porphyry ore deposits. *J. Geochem. Explor.* 152, 10–26.
- Wilkinson, J.J., Cooke, D.R., Baker, M.J., Chang, Z.S., Wilkinson, C.C., Chen, H.L., Fox, N., Hollings, P., White, N.C., Gemmell, J.B., Loader, M.A., Pacey, A., Sievwright, R.H., Hart, L.A., Brugge, E.R., 2017. Porphyry indicator minerals and their mineral chemistry as vectoring and fertility tools. Application of Indicator Mineral Methods to Bedrock and Sediments, 67–77.
- Williamson, B.J., Herrington, R.J., Morris, A., 2016. Porphyry copper enrichment linked to excess aluminium in plagioclase. *Nat. Geosci.* 9 (3), 237–241.
- Williamson, B.J., Hodgkinson, M., Imai, A., Takahashi, R., Armstrong, R.N., Herrington, R.J., 2018. Testing the plagioclase discriminator on the GEOROC database to identify porphyry-fertile magmatic systems in Japan. *Resour. Geol.* 68, 138–143.
- Xie, G., Mao, J., Zhao, H., 2011. Zircon U-Pb geochronological and Hf isotopic constraints on petrogenesis of Late Mesozoic intrusions in the southeast Hubei Province, Middle-Lower Yangtze River belt (MLYRB), East China. *Lithos* 125 (1–2), 693–710.
- Xie, G.Q., Zhu, Q.Q., Yao, L., Wang, J., Li, W., 2013. Discussion on regional metal mineral deposit model of late Mesozoic Cu–Fe–Au polymetallic deposits in the southeast Hubei province. *Bull. Mineral. Petrol. Geochem.* 32, 418–426 in Chinese with English abs.
- Xie, G.Q., Mao, J.W., Zhu, Q.Q., Yao, L., Li, Y.H., Li, W., Zhao, H.J., 2015. Geochemical constraints on Cu–Fe and Fe skarn deposits in the Edong district, Middle-Lower Yangtze River metallogenic belt, China. *Ore Geol. Rev.* 64, 425–444.
- Zeng, L.-P., Zhao, X.-F., Li, X.-C., Hu, H., McFarlane, C., 2016. In situ elemental and isotopic analysis of fluorapatite from the Taocun magnetite-Apatite deposit, Eastern China: constraints on fluid metasomatism. *Am. Mineral.* 101 (11), 2468–2483.
- Zhang, S., Chu, G., Cheng, J., Zhang, Y., Tian, J., Li, J., Sun, S., Wei, K., 2020. Short wavelength infrared (SWIR) spectroscopy of phyllosilicate minerals from the Tonglushan Cu–Au–Fe deposit, Eastern China: new exploration indicators for concealed skarn orebodies. *Ore Geol. Rev.* 122, 103516.
- Zhang, W., Jiang, S.-Y., Ouyang, Y., Zhang, D.i., 2021b. Geochronology and textural and compositional complexity of apatite from the mineralization-related granites in the world-class Zhuxi W–Cu skarn deposit: a record of magma evolution and W enrichment in the magmatic system. *Ore Geol. Rev.* 128, 103885.
- Zhang, S., Ma, Q., Chen, H., Long, X., Chu, G., Zhang, W., Cheng, J., Tian, J., 2021a. Petrogenesis of Early Cretaceous granitoids and mafic microgranular enclaves from the giant Tonglushan Cu–Au–Fe skarn orefield, Eastern China. *Lithos* 392–393, 106103.
- Zhang, F., Williamson, B.J., Rollinson, G.K., Hughes, H.S.R., 2023. A mineralogical investigation into the formation of ore-barren endoskarn: an example from the Tonglushan porphyry system, eastern China. *Ore Geol. Rev.* 157, 105441.
- Zhao, Y.M., Lin, W.W., Bi, C.S., Li, D.X., Jiang, C.J., 1990. Skarn Deposits of China. Geological Publishing House, Beijing, pp. 1–354 in Chinese.
- Zhao, H., Xie, G., Wei, K., Ke, Y., 2012. Mineral compositions and fluid evolution of the Tonglushan skarn Cu–Fe deposit, SE Hubei, east-central China. *Int. Geol. Rev.* 54 (7), 737–764.
- Zheng, J.H., Shen, P., Feng, W.Y., 2022. Hydrothermal apatite record of ore-forming processes in the Hatu orogenic gold deposit, West Junggar, Northwest China. *Contrib. Mineral. Petro.* 177, 27.
- Zhong, S., Feng, C., Seltmann, R., Li, D., Dai, Z., 2018. Geochemical contrasts between Late Triassic ore-bearing and barren intrusions in the Weibao Cu–Pb–Zn deposit, East Kunlun Mountains, NW China: constraints from accessory minerals (zircon and apatite). *Miner. Deposita* 53 (6), 855–870.
- Zhou, R.J., Wen, G., Li, J.W., Jiang, S.Y., Hu, H., Deng, X.D., Zhao, X.F., Yan, D.R., Wei, K.T., Cai, H.A., Shang, S.C., Li, B.C., Dai, X.K., 2022. Apatite chemistry as a petrogenetic–metallogenetic indicator for skarn ore-related granitoids: an example from the Daye Fe–Cu–(Au–Mo–W) district, Eastern China. *Contrib. Mineral. Petro.* 177, 23.
- Zhu, J.-J., Hu, R., Bi, X.-W., Hollings, P., Zhong, H., Gao, J.-F., Pan, L.-C., Huang, M.-L., Wang, D.-Z., 2022. Porphyry Cu fertility of eastern Paleo-Tethyan arc magmas: evidence from zircon and apatite compositions. *Lithos* 424–425, 106775.